國立臺灣大學電機資訊學院光電工程學研究所

碩士論文

Graduate Institute of Photonics and Optoelectronics

College of Electrical Engineering and Computer Science

National Taiwan University

Master's Thesis

矽 (110) 侷限效應在低溫環境下電子傳輸情形之研究

Study of 2D Electron Transport in Silicon (110) Confinement under the Cryogenic Environment

黃信雯

Hsin-Wen Huang

指導教授: 吳育任 博士

Advisor: Yuh-Renn Wu, Ph.D.

中華民國 113 年 8 月

August, 2024

doi:10.6342/NTU202404100

Acknowledgements

首先，十分感謝我的指導教授吳育任老師。剛進碩班的時候，對於元件物理方面只有薄弱的認知，而這段日子裡在一次次與老師的討論中，反覆思考物理與訓練研究分析問題的能力；除此之外，老師也很有耐心地協助我解決問題，過程中時常覺得物理圖像上的思考與理解十分有趣，非常感謝老師的教導。另外，還很感謝陳建宏經理的協助，在模型建立的路上，提供許多經驗與研究方向上的建議，讓我的研究得以更加完善。

感謝實驗室的同學、學長姐、學弟妹，陪我度過實驗室的時光，聊天吃飯的過程可以順便幫自己充電。感謝允平從大四下開始就時常與我討論模擬或是物理問題，常覺得是能力出眾的你帶領我一同解決問題。還謝謝名盛與緯榮，常陪我聊天舒緩心中的緊張與壓力。特別感謝靖容，不只關心我的生活，還給我許多良好的建議，時不時給予協助分擔我心裡的重量，讓我在研究的路上繼續往前。

感謝我的家人，謝謝父母讓我能無後顧之憂地攻讀碩士，全力支持著我並時常關心我的近況，是我最強而有力的後盾。

最後感謝國科會計畫編號 NSTC111-2923-E-002-009-, 111-2221-E-002-075-, 112-2221-E-002-215-MY3, 112-2221-E-002-214-MY3 的支持完成這本論文。

doi:10.6342/NTU202404100

摘要

本研究主要分析矽（110）侷限系統在低溫下電子傳輸情形。常溫下，載子之傳輸特性主要受聲子散射影響；有別於常溫，低溫下的載子傳輸須額外考慮進表面粗糙散射、遠程庫倫散射、雜質散射之影響。因此，文中首先根據量子效應計算出矽（110）侷限系統之子帶資訊，計算出材料聲子散射率，介電層所貢獻的遠程聲子散射率、表面粗糙散射率、遠程庫倫散射率、雜質散射率，讚以蒙地卡羅法評估出各條件下的電子遷移率。發現隨溫度調降，除表面粗糙散射數值不隨之改變外，其餘散射機制散射率皆隨溫度變小，原因為聲子佔居比例的下降，與固定通道載子濃度下屏蔽效應隨溫度下降的提升；因此，在此過程中，表面粗糙散射所佔的比例越來越高。除此之外，文中亦討論不同載子濃度下電子遷移率的變化。當通道載子濃度的低時，屏蔽效應減弱，遠程庫倫散射所佔比例提升；而隨載子濃度上升，屏蔽效應增強，遠程庫倫散射機制下降，以致電子遷移率升高；而再隨載子濃度越趨提升，電子分佈越靠近材料界面，因此電子受表面粗糙散射影響程度變得顯著，導致電子遷移率再次下降，最後得凹口向下的電子遷移率隨載子濃度分佈的趨勢。而此研究建立之低溫模型可推廣至其他系統，協助對該系統下載子遷移率的分析以及成因之釐清。

關鍵字：低溫系統、載子遷移率、矽（110）侷限系統、蒙地卡羅法

doi:10.6342/NTU202404100

Abstract

This study primarily analyzes the electron transport properties in silicon (110) confinement systems at low temperatures. At room temperature, the transport characteristics of carriers are mainly influenced by phonon scattering. However, unlike at room temperature, carrier transport at low temperatures must additionally consider the effects of surface roughness scattering, remote Coulombic scattering, and impurity scattering. Therefore, this paper first calculates the subband information of the silicon (110) confinement system based on quantum effects, and computes the phonon scattering rate of the material, the remote phonon scattering rate contributed by the dielectric layer, the surface roughness scattering rate, the remote Coulomb scattering rate, and the impurity scattering rate. Using the Monte Carlo method, the electron mobility under various conditions is evaluated. It is found that, as the temperature decreases, the scattering rates of all mechanisms except for surface roughness scattering decrease due to the reduction in phonon occupation and the enhancement of the screening effect at a fixed channel carrier concentration.

doi:10.6342/NTU202404100

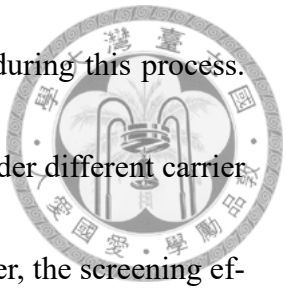

Therefore, the proportion of surface roughness scattering increases during this process. Besides, this paper also discusses the changes in electron mobility under different carrier concentrations. When the channel carrier concentration becomes lower, the screening effect weakens, and the proportion of remote Coulombic scattering increases. As the carrier concentration increases, the screening effect strengthens, and the remote Coulombic scattering mechanism decreases, resulting in an increase in electron mobility. However, as the carrier concentration continues to rise, the electron distribution moves closer to the material interface, making the impact of surface roughness scattering more significant, leading to a decrease in electron mobility again. This results in a downward concave trend of electron mobility with respect to carrier concentration. The low-temperature model established in this study can be extended to other systems, helping the analysis and clarification of carrier mobility and its causes in those systems.

Keywords: Cryogenic system, Mobility, Silicon (110) confinement, Monte Carlo method

doi:10.6342/NTU202404100

Contents

doi:10.6342/NTU202404100

doi:10.6342/NTU202404100

doi:10.6342/NTU202404100

List of Figures

doi:10.6342/NTU202404100

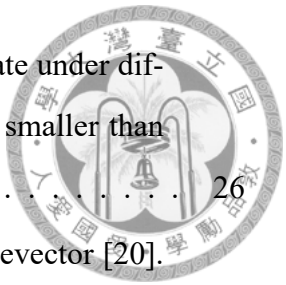

doi:10.6342/NTU202404100

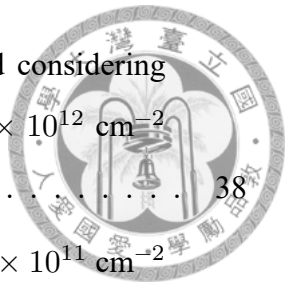

doi:10.6342/NTU202404100

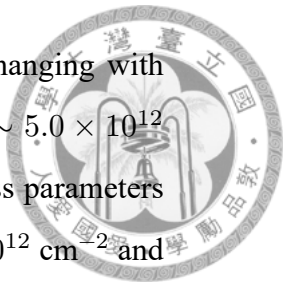

doi:10.6342/NTU202404100

List of Tables

doi:10.6342/NTU202404100

Chapter 1

Introduction

1.1 Motivation

With technological advancements, humans need to expand their understanding of physical mechanisms in low-temperature environments in order to utilize them more effectively [1]. For high-orbit satellite communication and quantum computer low-temperature circuit design, there are specific requirements. Semiconductor components need to operate within an extremely low-temperature range, where their characteristics undergo significant changes. For quantum computers, reducing thermal interference on qubits is crucial. Whether the qubits are primarily based on superconductors or silicon-based quantum dots, they operate at temperatures ranging from ten to thousand mK. Additionally, to control these superconducting qubits, both operational and reading circuits operate near 4 K. Considering cooling power consumption, they may also be designed to operate near 77 K. Therefore, understanding the characteristics of components at low temperatures becomes critical.

doi:10.6342/NTU202404100

1.2 Carrier Transport under the Cryogenic System

At room temperature, the phonon is the main reason causing the carriers to scatter[2]. However, at the cryogenic temperature, the thermal energy of the system is significantly reduced, leading to distinct interactions with impurities, remote charges, and surface roughness. Therefore, the scattering mechanisms, including acoustic phonon scattering, optical phonon scattering, remote phonon scattering, ionized impurity scattering, remote Coulombic scattering, surface roughness scattering, and interface scattering, play crucial roles in determining the overall carrier mobility. Understanding these mechanisms is essential for optimizing the design and performance of semiconductor devices operating under cryogenic conditions.

1.3 Simulation of the Transport Properties

There are two methods are usually used in estimating the electron mobility. There are the Boltzmann Transport Equation (BTE) [3] and the Monte Carlo (MC) [4] method. The Boltzmann transport equation is a classical approach that describes the statistical behavior of particles under the influence of external forces and collisions. It provides a deterministic framework for calculating the distribution function of carriers. The BTE can be expressed as:

$$\frac{\partial f}{\partial t} + \mathbf{v} \cdot \nabla_{\mathbf{r}} f + \mathbf{F} \cdot \nabla_{\mathbf{k}} f = \left(\frac{\partial f}{\partial t} \right)_{\text{collision}}, \tag{1.1}$$

where f is the distribution function, $\mathbf{v}$ is the carrier velocity, $\mathbf{F}$ is the external force, and the right-hand side represents the collision term. On the equation left-hand side, $\mathbf{v} \cdot \nabla_{\mathbf{r}} f$ represents the diffusion motion and $\mathbf{F} \cdot \nabla_{\mathbf{k}} f$ depicts the drift motion. As solving the BTE,

doi:10.6342/NTU202404100

the relaxation time approximation or iterative methods is required, to account for various scattering mechanisms.

In contrast, the Monte Carlo method is an approach that simulates the trajectories of individual carriers through random sampling of scattering events. This method involves initializing the carriers with specific energy and momentum, propagating them through the material, and accounting for interactions with phonons, impurities, remote charges, and interfaces. The MC method provides a detailed, microscopic view of carrier dynamics, and it can capture the effects of rare but significant scattering events.

Comparing these two methods, the BTE is a more straightforward and less computationally intensive approach for systems where the scattering mechanisms can be well-approximated. However, it may oversimplify complex interactions. On the other hand, the Monte Carlo method, while computationally demanding, provides a more accurate and detailed simulation of carrier transport, especially in systems with complex and multiple scattering mechanisms. Therefore, to accurately model the carrier transport properties at low temperatures, we apply the Monte Carlo method in the simulation. We aim to provide a comprehensive understanding of the transport properties. The analysis will help identify the dominant scattering mechanisms and their impact on carrier mobility.

1.4 Silicon (1 1 0) Confinement FinFET

Nowadays, as the gate length becomes shorter, gate control becomes more difficult. Replacing the planar FET, the FinFET structure is commonly used to enhance the control of the gate. Owing to the advance in fabrication techniques, the channel width of the FinFET has the ability to reach several nanometers. Based on this structure, the system

doi:10.6342/NTU202404100

can be seen as a quantum well. The confinement of carriers in the narrow fin structure leads to enhanced electrostatic control and reduced short-channel effects. However, the confined geometry also emphasizes the impact of scattering mechanisms, making it vital to thoroughly understand and reduce these effects.

(110) oriented FinFETs show exceptional potential for performance improvement through strain engineering, making them promising for future high-performance electronic devices [5]. Fig. 1.1 shows the layout of (110)/[1$\bar{1}$0] and (010)/[100] FinFETs fabricated on a (001) silicon wafer. In their research, (110)/[1$\bar{1}$0] FinFET has a better ability to improve electron mobility compared with the (010)/[100] one. The combination of compressive strain along the fin height and tensile strain along the fin width or compressive strain along the fin width can enhance electron mobility. Therefore, studying carrier transport in silicon (110) confinement FinFETs at low temperatures provides valuable insights into optimizing these devices for advanced applications.

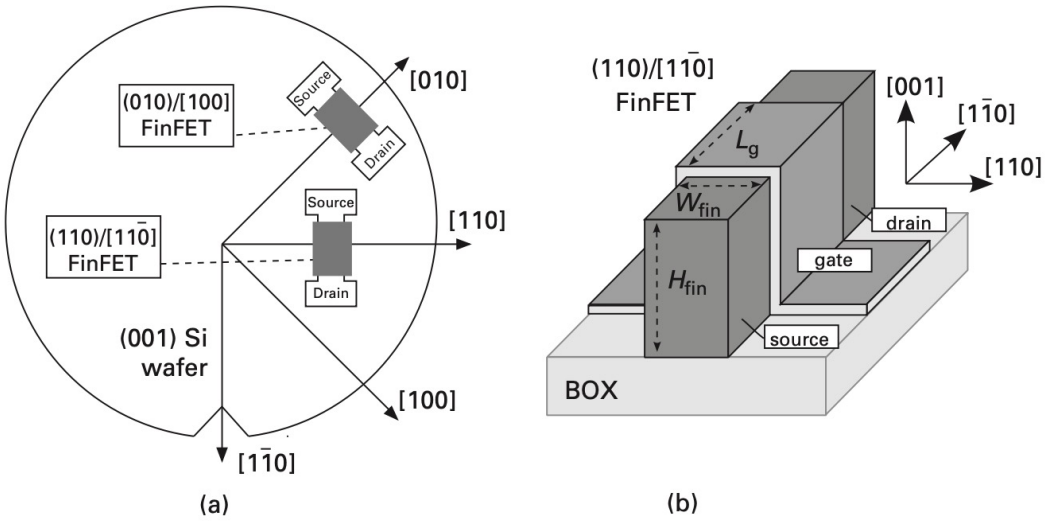

Figure 1.1: (a) Layout of (110)/[1$\bar{1}$0] and (010)/[100] FinFETs fabricated on a (001) silicon wafer. (b) Sketch of the device and an indication of the transport and quantization directions for a FinFET oriented along the [1$\bar{1}$0] direction.

doi:10.6342/NTU202404100

1.5 Thesis overview

This thesis aims to investigate the carrier mobility in low-temperature silicon (110) confinement systems by analyzing the contributions of various scattering mechanisms. Therefore, in chapter 2, the various scattering mechanisms are mentioned. The physical picture of these scattering process and the derivation of the scattering rates are explained. Also, the steps of Monte Carlo method we used is introduced. Further, in chapter 3, the subband separation calculation result of silicon (1 1 0) confinement system is shown. Based on the effective mass, eigen value, and wavefunction we obtained, the magnitude of the scattering rates of every mechanisms are estimated. Moreover, the mobilities with various temperatures is acquired by the Monte Carlo method. In the end, the aforementioned results are discussed. In chapter 4, the conclusion of this thesis is made. The new findings of this research and suggestion directions for future study are summarized.

doi:10.6342/NTU202404100

Chapter 2

Methodology

2.1 Overview

In this chapter, we first introduce the valley information of the silicon (110) confinement system. The effective mass in different directions of projected valleys is shown, and there are two types, Δ-4 and Δ-2, of these valleys [6]. Otherwise, in the quantum well, the electron behaves like a wave. Therefore, the Poisson equation and Schrödinger equation solver are applied to obtain the wave functions.

Further, we discuss the physical picture of each scattering mechanism under the cryogenic system since as the temperature decreases, the influence of the phonon-induced scattering is reduced. Instead, we have to consider surface roughness scattering, remote Coulombic scattering, and impurity scattering in our simulation model. Therefore, the methodologies used to calculate the scattering rate of every mechanism are derived and explained as follows. Finally, the multi-valley Monte Carlo model is utilized to evaluate the mobility of the electron mobility.

doi:10.6342/NTU202404100

2.2 Scattering Mechanism

As the carrier transports through the material, the scattering happens, since the lattice vibration or the Coulomb force from other charges. The trajectory of carriers changes after interacting with the phonon or the scattering potential (Fig. 2.1). Scattering can be seen as a perturbation, and Fermi's Golden rule[7, 8] is applied to derive the scattering rate of each scattering mechanism. Fermi's Golden Rule is Eq. 2.1:

$$W(k,k') = \frac{2\pi}{\hbar} |M_{kk'}|^2 \delta(E_{k'} - E_k), \tag{2.1}$$

where $W(k,k')$ is the scattering rate of the transition in which the initial state is k and the final state is k', $M_{kk'}$ is the matrix element of the scattering, E_k is the initial carrier energy, and $E_{k'}$ represents the final energy after the scattering.

The scattering mechanisms discussed in this paper can be classified into two categories, elastic scattering, and inelastic scattering. In the elastic scattering, the carrier energy is conserved. In this group, there are acoustic phonon scattering, surface roughness scattering, remote Coulombic scattering, and ionized impurity scattering. Moreover, inelastic scattering involves the process of energy absorption and emission. In this category, there are optical phonon scattering, intervalley scattering, and remote phonon scat-

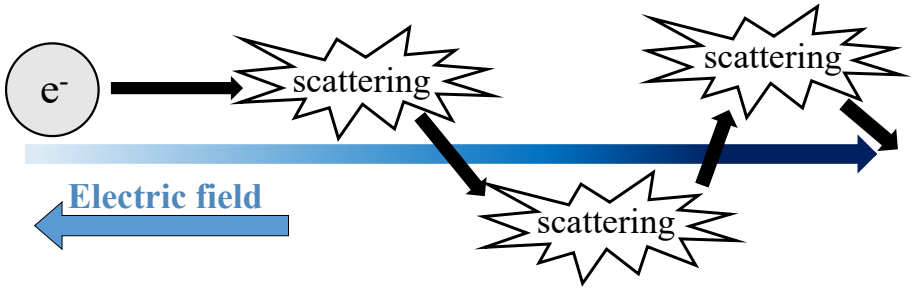

Figure 2.1: An electron transports in the material and scattering events happen.

doi:10.6342/NTU202404100

tering. During these scattering mechanisms, the momentum conservation of electrons and phonons is considered. Therefore, the changing of the phonon wave vector resulting from the initial and final state of electron scatter are calculated. In the further session, based on the silicon (1 1 0) confinement system, the scattering rate derivation of every scattering mechanism is shown, and the formation of the matrix element is discussed.

2.3 Acoustic Phonon Scattering

In the real lattice, due to the heat fluctuation, the atoms vibrate around their equilibrium position. As the atoms move away from the equilibrium site, the strain in the lattice is caused. This strain impacts the motion of electrons. Therefore, the vibration of the lattice is considered as a kind of particle ”phonon”, which causes the carrier scattering. In general, phonon can be classified into two types, acoustic phonon and optical phonon. The difference between these two types is the direction of atoms' vibration (Fig. 2.2). As the atoms move in the same direction, the strain energy in the lattice is caused. This nature is called acoustic phonon. The electronic energy perturbation is related to the strain in the

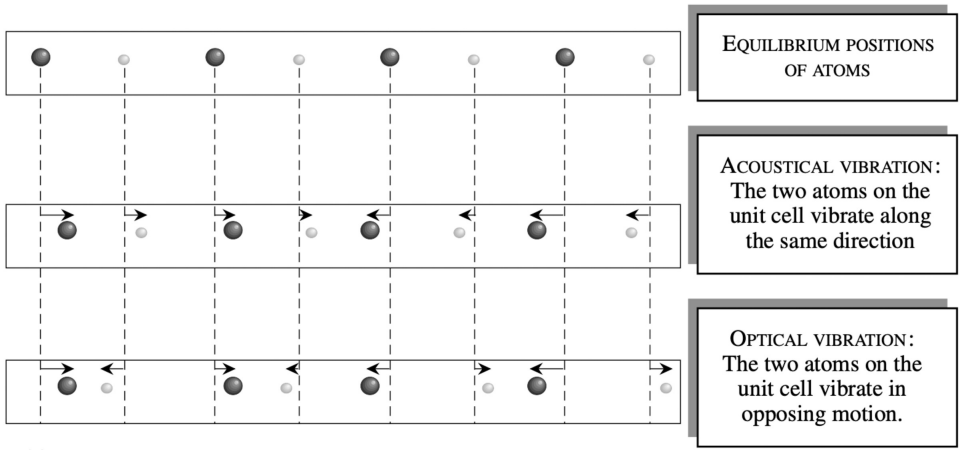

Figure 2.2: The vibration of acoustic phonon and Optical phonon [9].

doi:10.6342/NTU202404100

crystal, and the perturbation potential can be described as

$$U_{ac} = D_{ac}\frac{\partial u}{\partial x} \tag{2.2}$$

where D_{ac} is the acoustic phonon deformation potential, and $\frac{\partial u}{\partial x}$ represents the displacement of two atoms. Accroding to the purterbation theory,

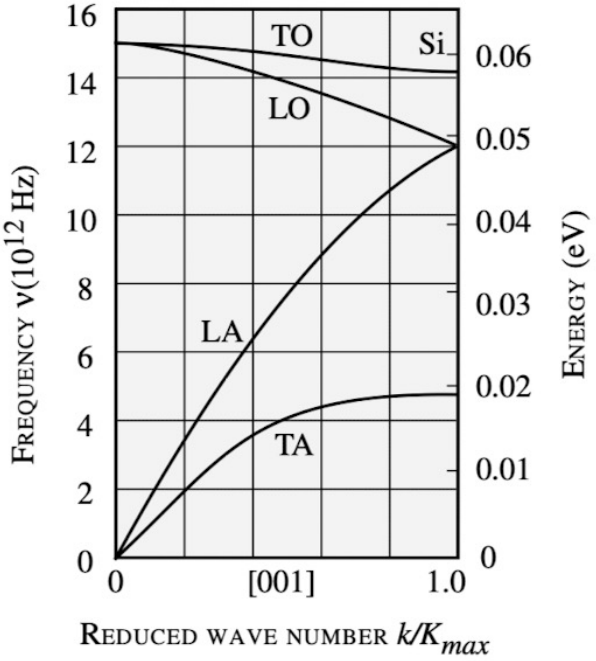

Figure 2.3: Phonon spectra of silicon [9].

Fig. 2.3 is the phonon branches of silicon. It represents the phonon energy distribution in the lattice. TA and LA are transversal acoustic phonon and longitudinal acoustic phonon separately. Around the zero momentum position, the energy of these two phonon types is close to zero. Therefore, acoustic phonon scattering can be seen as the elastic collision between the electron and phonon. In addition, in this case, the phonon occupation

$$n(\omega) = \frac{1}{exp(\frac{\hbar\omega}{k_B T}) - 1} \tag{2.3}$$

doi:10.6342/NTU202404100

is approximated to

$$n(\omega) = \frac{\hbar\omega}{k_B T} \tag{2.4}$$

since the small phonon energy. Further, with the band structure and phonon spectra, the acoustic phonon scattering rate can be described as

$$W_{ac}(k) = \pi \frac{k_B T D_{ac}^2}{\rho v_s^2 \hbar} N_{2D}(E_k)/L \tag{2.5}$$

where k_B is Boltzmann constant, T is temperature, D_{ac} is the deformation potential of acoustic phonon, ρ is the mass density, v_s is the sound velocity, N_{2D} is the 2D density of state, and L is the width of the system.

2.4 Optical Phonon Scattering

As atoms in the same unit cell vibrate in the opposite direction, this type of vibration is called optical phonon (Fig. 2.2). Optical phonon has larger energy compared with the acoustic one. This vibration also caused the strain in the lattice, and the strain is proportional to the displacement of atoms. The perturbation potential can be described as

$$U_{op} = D_{op} u \tag{2.6}$$

where D_{op} is the optical phonon deformation potential, and u is the relative displacement of two atoms. As Fig. 2.3 shows, LO and TO are the optical phonon branches. In addition, at the zero momentum, the optical phonon still has its energy (Fig. 2.3). Therefore, the calculation of phonon occupation can not be approximated to Eq. 2.4. Then, the optical

doi:10.6342/NTU202404100

phonon scattering rate is written as,

$$W_{op}(k) = \frac{\pi D_{op}^2}{2\rho\omega_0}\left[n(\omega_0) + \frac{1}{2} \mp \frac{1}{2}\right] N_{2D}(E_k \pm \hbar\omega_0)/L \tag{2.7}$$

In the phonon absorption scattering rate derivation, the phonon occupation is $n(\omega_0)$. On the other hand, if phonon emission mechanism is calculated, the phonon occupation is $n(\omega_0) + 1$.

2.5 Equivalent Intervalley Phonon Scattering

After interacting with the aforementioned phonon, the carriers have the probability to scatter into other valley. In this process, the momentum between electron and phonon is conserved. In silicon, there are six equivalent X-valleys. Fig. 2.4 shows the electron equivalent intervalley scattering transition. If the electron scatters into the opposite valleys ($< 100 >$ scatter to $< \bar{1}00 >$), this transition is called g-type scattering. The additional phonon wavevector in g-type transition involves the 0.3 times zone edge magnitude. On the other hand, if the electron scatters into the non-opposite valleys ($< 100 >$ scatter to

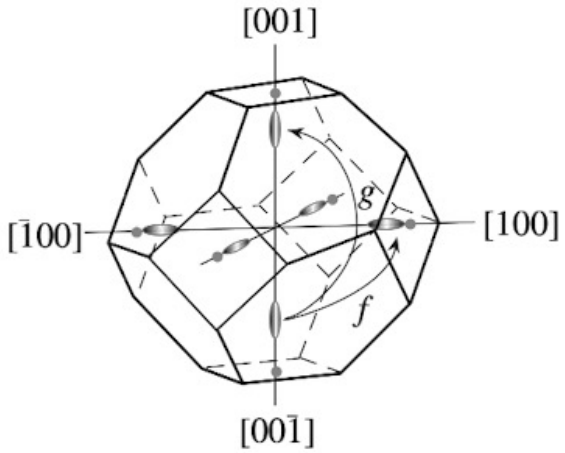

Figure 2.4: Silicon equilibrium intervalley scattering. There are six equivalent valleys at the conduction band edge, and the g-type and the f-type scattering is shown [9].

doi:10.6342/NTU202404100

$< 010 >$), this transition is called f-type scattering. The additional phonon wavevector in f-type transition requires a zone edge magnitude.

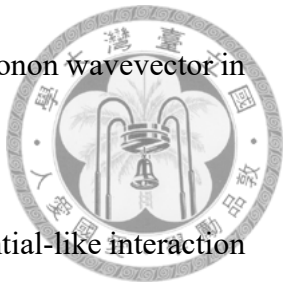

This scattering mechanism can be modeled by deformation potential-like interaction

$$U_{ep} = D_{if}u \tag{2.8}$$

where D_{if} is the intervalley deformation potential, and i and f represent the electon scatters from i to f valley. Then, the scattering rate can be written as

$$W_{ep}(k) = \frac{\pi D_{ac/op}^2}{2\rho\omega_0}[n(\omega_{ac/op}) + \frac{1}{2} \mp \frac{1}{2}]N_{2D}(E_k \pm \hbar\omega_{ac/op})/L \tag{2.9}$$

where footnote ac and op represent the acoustic phonon caused and optical phonon caused intervalley scattering, respectively.

2.6 Remote Phonon Scattering

The dielectric layer around the channel supports polar vibration modes, and the motion of the carrier in the channel is influenced. This scattering mechanism is called remote phonon scattering or surface-optical phonon scattering[10, 11]. If the high-k dielectric material is used, the influence of remote phonon will be severe. Therefore, this scattering mechanism should be considered in this thesis.

The process of remote phonon scattering is an inelastic collision, and it is strongly related to the material used as the dielectric layer. The electron-phonon coupling strength is [11, 12]

$$F^2 = \frac{\hbar\omega_{so}}{2A\epsilon_0}(\frac{1}{\epsilon_{top}^{\infty} + \epsilon_{bot}^{\infty}} - \frac{1}{\epsilon_{top}^{0} + \epsilon_{bot}^{0}}), \tag{2.10}$$

doi:10.6342/NTU202404100

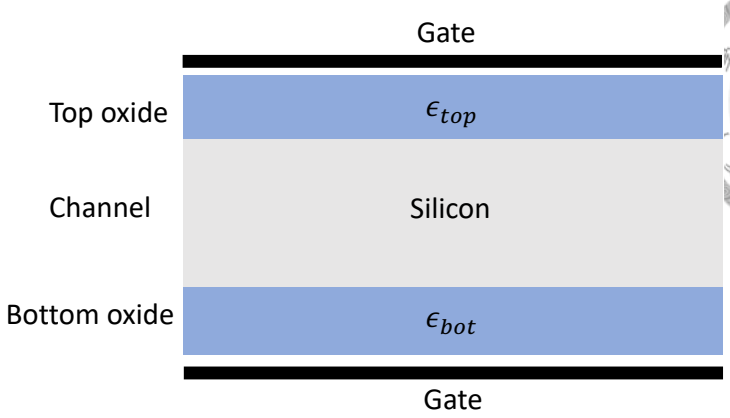

Figure 2.5: Schematic of the double gate device and the meaning of ϵ_{top} and ϵ_{bot} .

where $\hbar\omega_{so}$ is the remote phonon energy, ϵ_{top}^{∞} is the high-frequency permittivity of the top dielectric layer, ϵ_{bot}^{∞} is the high-frequency permittivity of the bottom dielectric layer, ϵ_{top}^{o} is the low-frequency permittivity of the top dielectric layer, and ϵ_{bot}^{o} is the low-frequency permittivity of the bottom dielectric layer. Fig. 2.5 depicts the device structure and the meaning of the top and bottom dielectric layers. In addition, if there are two remote phonon types, F^2 should be written as

$$F_1^2 = \frac{\hbar\omega_{so1}}{2A\epsilon_0}\left(\frac{1}{\epsilon_{top}^{int}+\epsilon_{bot}^{int}} - \frac{1}{\epsilon_{top}^{0}+\epsilon_{bot}^{0}}\right), \tag{2.11}$$

$$F_2^2 = \frac{\hbar\omega_{so2}}{2A\epsilon_0}\left(\frac{1}{\epsilon_{top}^{\infty}+\epsilon_{bot}^{\infty}} - \frac{1}{\epsilon_{top}^{int}+\epsilon_{bot}^{int}}\right), \tag{2.12}$$

where ϵ_{top}^{int} is the intermediate permittivity of the top dielectric, and ϵ_{bot}^{int} is the intermediate permittivity of the bottom dielectric. A is the area. The remote phonon frequency ω_{so} is

$$\omega_{so1} = \omega_{TO1}\sqrt{\frac{\epsilon_{top}^{0}+\epsilon_{bot}^{\infty}}{\epsilon_{top}^{int}+\epsilon_{bot}^{\infty}}}, \tag{2.13}$$

$$\omega_{so2} = \omega_{TO2}\sqrt{\frac{\epsilon_{top}^{int}+\epsilon_{bot}^{\infty}}{\epsilon_{top}^{\infty}+\epsilon_{bot}^{\infty}}}. \tag{2.14}$$

where ω_{TO1} and ω_{TO2} are the transversal optical phonon frequency of the dielectric. The

doi:10.6342/NTU202404100

remote phonon scattering rate is

$$W_{rp}(k) = \frac{2\pi}{\hbar}\int \frac{e^2F^2}{\epsilon(q,w)^2}\frac{exp(-2qd)}{2q}dq[n(\omega_0)+\frac{1}{2}\mp\frac{1}{2}]N_{2D}(E_{k'}-E_k\pm\hbar\omega_0) \quad (2.15)$$

q is the phonon wave vector which is related to the angle and the magnitude of $k^{'}$ and k. d is the distance between the remote phonon and channel carrier, e is the modulus of the electron charge, and $\epsilon(q,w)$ is the static screening of the material, which is

$$\epsilon(q,w) = 1 + v_c(q)\Pi(q,w), \quad (2.16)$$

where v_c is $\frac{e^2}{2\hat{k}q}$, $\hat{k} = \frac{\epsilon^0_{top}\epsilon^0_{bot}}{2}$, and $\Pi(q,w)$ is approximated as $\frac{m^*}{\pi\hbar^2}$.

2.7 Remote Coulombic Scattering

Remote Coulombic scattering occurs when carriers in the channel interact with charged impurities or defects located in the oxide layer or at the oxide-semiconductor interface. These remote charges create a Coulomb potential that perturbs the motion of the carriers, leading to scattering events and degrading the carrier mobility (Fig. 2.6). Moreover, in this scattering process, the interaction is elastic. The scattering rate due to remote Coulombic interactions can be derived using Fermi's Golden Rule. The rule provides the transition

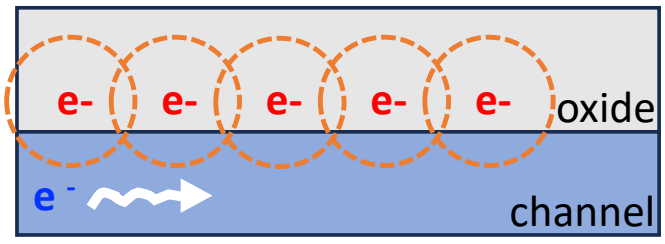

Figure 2.6: The schematic of remote Coulombic scattering[13, 14]. The formation of the Coulomb potential (orange dashed line) of charges in oxide (red) influences the channel carrier (blue) transport.

doi:10.6342/NTU202404100

rate for an electron due to an external perturbation. For Coulombic scattering, the perturbation potential $V(\mathbf{r})$ is given by the Coulomb potential of the charges. After the Fourier transform, the potential is written as [15]

$$V(Q,z) = \frac{f_Q}{2Q\epsilon_0\epsilon_s}[e^{-Q(z-z_0)} - \frac{S_v}{Q+S_v} \times e^{-Q|z-z_I|} \times e^{-Q(z_I-z_0)}]. \tag{2.17}$$

where $Q = |k^{'} - k|$, k and $k^{'}$ are the final and initial state of the electron wavevector, z is the direction vertical perpendicular to oxide-semiconductor interface, z_0 is the location of the charges in the oxide, z_I is the position of electron wavefunction maximum, ϵ_0 is the vacuum permittivity, ϵ_s is the dielectric constant of the semiconductor, f_Q is a constant solved from the boundary condition and S_v is the screening parameter. The screening parameter in a two-dimensional electron gas is

$$S_v = \frac{e^2}{2\epsilon_0\epsilon_s}\frac{n_v}{k_B T} \tag{2.18}$$

where n_v is the carrier density. In addition, in Eq. 2.17, the first term on the right-hand side represents the Coulomb effect from the charges in oxide, and the second term describes the screening effect of the carriers in the channel. Then, the matrix element is

$$|M(\vec{k},\vec{k'})|^2 = |\langle\vec{k}|e \times V(Q,z)|\vec{k'}\rangle|^2. \tag{2.19}$$

According to Fermi's golden rule, the scattering rate is expressed as

$$W_{RCS}(k) = \frac{2\pi}{\hbar}\int |M(\vec{k},\vec{k'})|^2 dk^{'}\delta(E_{k'} - E_k)N_{fix}. \tag{2.20}$$

where N_{fix} is the 2D fix-charge density in oxide.

Moreover, the Coulomb-force-related scattering is an angular-dependent mechanism.

doi:10.6342/NTU202404100

If the screening effect is weak, the system has a small angle scattering preference. If the screening effect is strong, the distribution of the scattering angle is closer to uniform. The scattering angle relation follows the calculation result of Eq. 2.20.

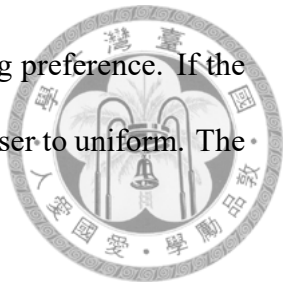

2.8 Impurity Scattering

Impurity scattering occurs when charge carriers interact with impurities or defects within the semiconductor lattice. These impurities (dopants or defects) create localized potentials that perturb the motion of the carriers, leading to scattering events. Impurity scattering is particularly important in determining the electrical properties of semiconductors at low temperatures or in highly doped materials [16].

The formation of the perturbation potential is similar to that in remote Coulombic scattering. Both of them resulted from the Coulombic force. Therefore, this scattering is an elastic process. The only difference is the position of the fixed charges. In terms of impurity scattering, the charges are located at the channel. Further, the scattering rate due to the impurities can be derived using Fermi's Golden Rule. Based on the Coulomb potential of the charged impurity, the matrix elements are written as

$$|M_{IMP}(\vec{k},\vec{k'})|^2 = |\langle\vec{k}|e \times V_{IMP}(Q,z)|\vec{k'}\rangle|^2. \tag{2.21}$$

Finally, according to Fermi's golden rule and integrating over all possible final states, the impurity scattering rate can be obtained

$$W_{IMP}(k) = \frac{2\pi}{\hbar}\int |M_{IMP}(\vec{k},\vec{k'})|^2 dk' \delta(E_{k'} - E_k) N_{IMP}. \tag{2.22}$$

where N_{IMP} is the density of ionized impurity. Finally, due to impurity scattering being

doi:10.6342/NTU202404100

oriented from the Coulombic force, this mechanism is also angular dependent, which is like remote Coulombic scattering.

2.9 Surface Roughness Scattering

The quality of the interface between two different materials depends on the fabrication process. In n-MOSFET, electrons travel in the inversion layer around the interface of oxide and channel material. During carrier transport, scatter events happen due to the imperfection interface, and this phenomenon is called surface roughness scattering[17]. The distribution of the roughness at the surface is assumed as a Gaussian distribution as Eq. 2.23 [18]

$$< \Delta(r)\Delta(r^{'} - r) >= \Delta^2 exp(-\frac{r^2}{\lambda^2}), \tag{2.23}$$

where Δ is the root-mean-square height of the surface roughness, λ is the correlation length of the surface roughness along the interface (Fig. 2.7). The scattering matrix ele-

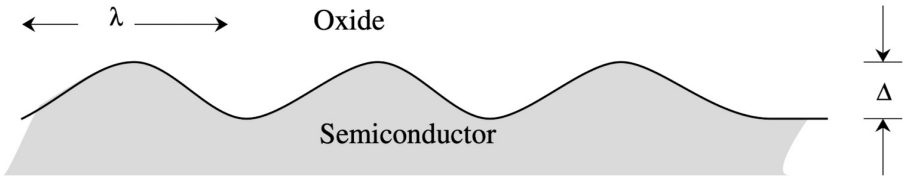

Figure 2.7: Schematic of the interface of oxide and semiconductor layer [9].

ment can be written as

$$M(k, k^{'}) = \int_{-\Delta z}^{\Delta z} \delta U(r, z)|\psi(z)|^2 dz, \tag{2.24}$$

where Δz is the distance away from the interface, δU is the difference of conduction band edge for oxide and semiconductor, and $\psi(z)$ is the wavefunction of the electrons in the inversion layer. This equation describes the probability of the electron around the surface

doi:10.6342/NTU202404100

and is influenced by the surface roughness. Further, according to Fermi's golden rule, the surface roughness scattering rate can be derived as

$$W_{SR}(k) = \frac{2\pi}{\hbar} \int |M_{kk'}|^2 dk' \delta(E_{k'} - E_k). \tag{2.25}$$

2.10 Monte Carlo Method

During the flight, the carrier collides with the phonon or is influenced by the Coulomb potential of other charges. Then, the scattering happens with the changing of electron momentum and velocity (Fig. 2.1). Within the scattering rate result of the above scattering mechanisms, a Monte Carlo model is built. Since the scattering event happens randomly, the Monte Carlo method is a profitable scheme to deal with the nature of scattering. The detailed steps of Monte Carlo are shown in Fig. 2.8.

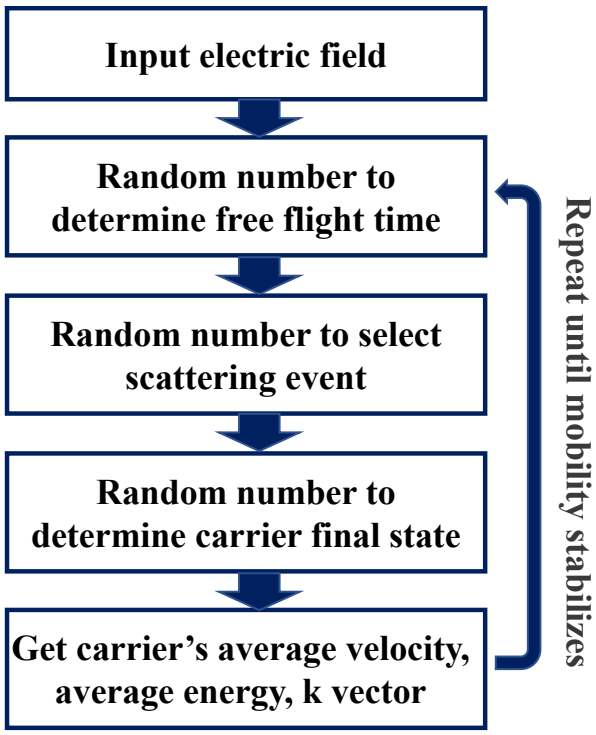

Figure 2.8: The flow chart of Monte Carlo method.

To begin with, assume there is an electron under a given electric field, and it is ac-

doi:10.6342/NTU202404100

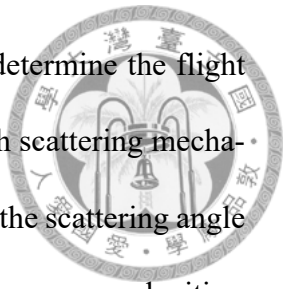

celerated at the same time. Next, a random number is generated to determine the flight interval. Further, a random number is generated again to decide which scattering mechanism is chosen. Then, the third random number is drawn to determine the scattering angle and the final state of the electron. Finally, the new momentum, carrier energy, velocities, and flight distance during the flight interval are recorded. The aforementioned steps are a loop for the Monte Carlo method. This process is repeated until the total flight time or total flight distance we set is satisfied. In the end, the average velocities of carriers and mobilities can be obtained.

2.11 Poisson, Drift-Diffusion, and Schrödinger Solver

In this research, the Poisson and drift-diffusion self-consistent model is used to perform the device simulation. The Poisson equation is used to describe the relation between carrier distribution and the potential. The Poisson equation is

$$\nabla\epsilon\nabla E_c = q(N_A^- - N_d^+ + n_e - p) \tag{2.26}$$

where E_c is the potential, N_A^- is the doping concentration of acceptor, N_d^+ is the doping concentration of donor, n_e is the electron concentration, and p is the hole concentration. As the system is applied by the bias, the band structure of the system is altered, and the carrier distribution changes. The drift-diffusion model is used to solve the current, and it is in the form of

$$J_n = -q\mu_n n_e \nabla V - qD_n \nabla n_e, \tag{2.27}$$

$$J_p = -q\mu_p p \nabla V + qD_p \nabla p, \tag{2.28}$$

doi:10.6342/NTU202404100

where J_n and J_p are the electron and the hole current, respectively. μ_n and μ_p are the electron and the hole mobility, respectively. D_n and D_p are the diffusion coefficients of electron and hole, respectively. In Eq. 2.27 and 2.28, the first term on the right-hand side means the drift current. The second term on the right-hand side represents the diffusion current, and it is related to the carrier concentration difference. As the bias is applied to the system, the Poisson equation and drift-diffusion equation are calculated iteratively until convergence is reached. Based on the potential result, the Schrödinger equation is solved and the wavefunction can be acquired.

doi:10.6342/NTU202404100

Chapter 3

Results and Discussion

3.1 Silicon (110) confinement system

Silicon, with its semiconductor properties and our mature fabrication technology, has been the cornerstone of modern electronic devices. As the device dimensions continue to scale down, the width of the FinFET channel becomes thinner. Compared with bulk silicon, which is typically characterized by its (100) crystal orientation, silicon (110) confinement systems have a different electronic property. When silicon is confined to nanoscale dimensions, quantum mechanical effects become significant, further altering its electronic properties. In silicon (110) confinement systems, carriers are confined within a thin silicon layer, typically a few nanometers thick, sandwiched between insulating layers. This confinement leads to the formation of quantum wells, where the motion of carriers is restricted in one or more dimensions. As a result, the energy levels become quantized, and the carrier mobility can be significantly enhanced due to the reduction of scattering.

Fig. 3.1 is the FinFET structure which we simply it into a quantum well, and the width of the quantum well is 5 nm. The FinFET channel is (110) orientation silicon, and

doi:10.6342/NTU202404100

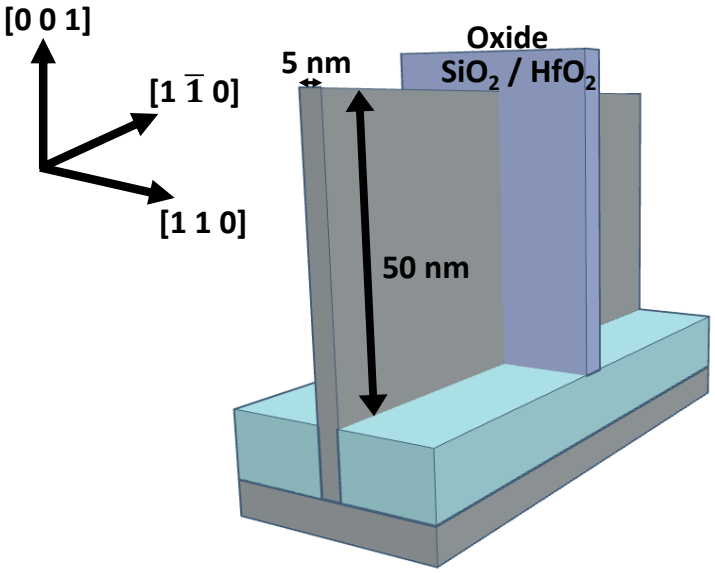

Figure 3.1: The structure of FinFET we simulate. The FinFET height is 50 nm and the FinFET width is 5 nm.

the oxide is SiO_2 or HfO_2 in further discussion.

3.1.1 Valleys in Conduction Band

Silicon has six same valleys in a lattice (Fig. 2.1); however, due to the confinement in (110) direction, the valleys separate into two types, Δ-4 and Δ-2 (Fig. 3.2). The electron effective mass also changes, and the value is shown in Table 3.1. Since the effective mass of Δ-4 valleys in the confinement direction is larger than that of Δ-2 valleys, Δ-4 has the lower energy in the first subband. Therefore, in our simulation, Δ-4 is the first valley. The lowest point of the band structure in the system is the first subband minimum of the Δ-4 valley.

Valley type	$m_{[1\bar{1}0]}/m_0$	$m_{[001]}/m_0$	$m_{confine}/m_0$
Δ-4	0.553	0.190	0.315
Δ-2	0.190	0.916	0.190

Table 3.1: Electron effective mass of various valleys [5]. $m_{[1\bar{1}0]}$ is the effective mass along $[1\bar{1}0]$ direction.

doi:10.6342/NTU202404100

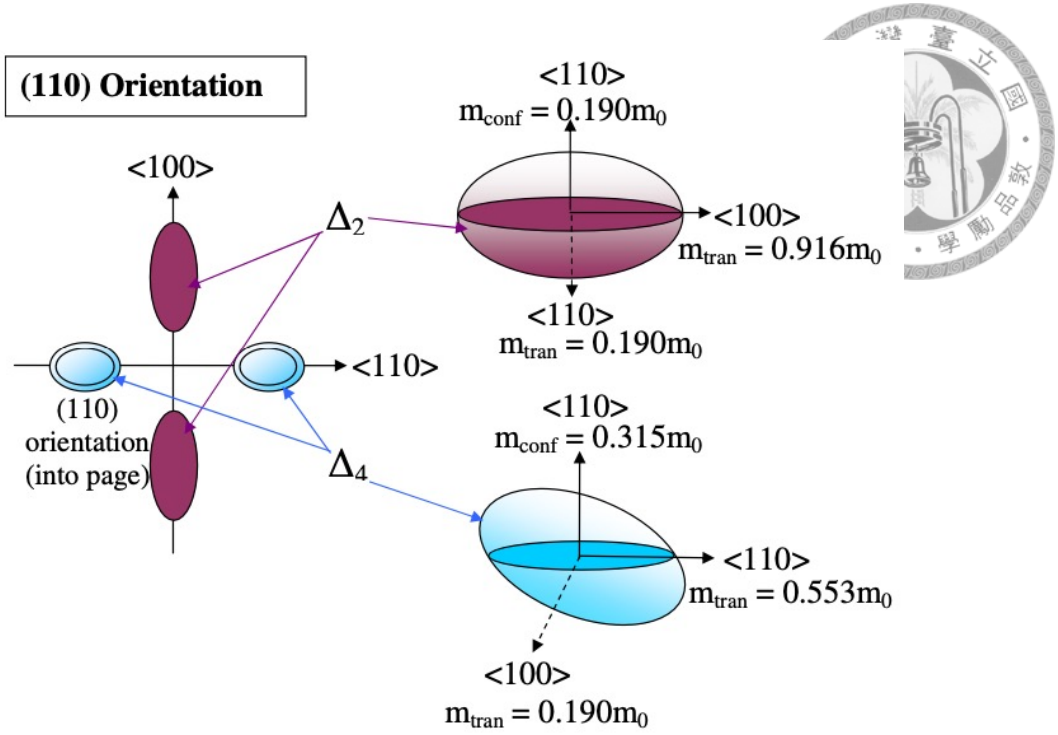

Figure 3.2: The constant energy surfaces of the silicon conduction band minima in (110) plane. [19]

3.2 Electron-phonon Scattering

Phonon-caused scattering is crucial when discussing the electron transport property. Since the phonon is oriented from the heat fluctuation, the electron-phonon scattering rate is highly related to the environment temperature. In this section, the effects of acoustic phonon, optical phonon, and remote phonon are mentioned, and the scattering rates under different temperatures are calculated. Moreover, by the Monte Carlo method, the field-dependent velocities and mobility of these scattering mechanisms can be obtained, and the results are discussed.

3.2.1 Acoustic Phonon Scattering

The acoustic phonon is the atoms in the lattice vibrate in the same direction, and the frequency is lower, compared with the optical phonon. Therefore, acoustic phonon has

doi:10.6342/NTU202404100

lower energy (Fig.2.3). There are two types of acoustic phonon: longitudinal acoustic phonon (LA) and transversal acoustic phonon (TA). According to the deformation potential theory, the sound velocity is required to calculate the acoustic phonon scattering rate. Sound velocity is acquired by fitting the linear part of the LA phonon around the small wavevector. In our calculation, the sound velocity v_s and the other parameters used in Eq. 2.5 are listed in Table. 3.2. The device in ref. [19] is like a tri-gates structure, and the D_{ac} the researcher used is 6.27 eV. However, in terms of SOI, Esseni found the value should be 14.6 eV [13], and this condition is more similar to our study. Therefore, 14.6 eV is chosen as D_{ac} in our further calculation.

Material	$D_{ac}(eV)$	$\rho_{Si}(kg/m^3)$	m_{eff} (m_o)	v_s (cm/s)	m_{dos} (m_o)
Si	6.27 / 14.6 [13]	9.54×10^3	0.553	9.54×10^5	0.324

Table 3.2: Parameters of silicon used in acoustic phonon scattering rate calculation. [19]

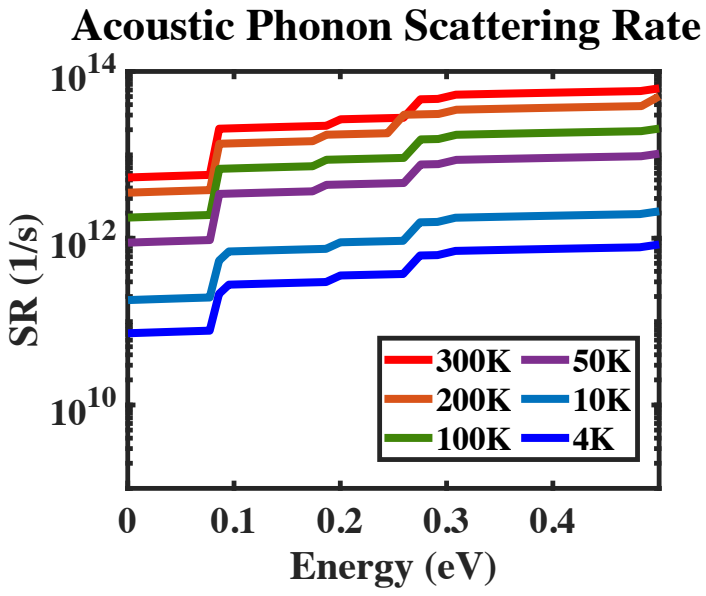

Figure 3.3: Acoustic phonon scattering rate under different temperatures.

Fig. 3.3 is the acoustic phonon scattering rate with different temperatures. As the temperature decreases, the scattering rate becomes lower. This means the scattering effect from acoustic phonon is smaller as temperature drops. Therefore, higher mobility in low

doi:10.6342/NTU202404100

temperature conditions is predicted.

3.2.2 Optical Phonon Scattering

The optical phonon is the atoms in the lattice that vibrate in the opposite direction, and the frequency is higher than the acoustic phonon. There are two types of optical phonon: longitudinal optical phonon (LO) and transversal optical phonon (TO). Based on the deformation potential theory and Eq. 2.7, Table. 3.3 is the required parameter used in the optical phonon scattering rate calculation.

Phonon mode	$D_{op}(eV/m)$	$\hbar\omega_{op}(eV)$
Optical	3.55×10^{10}	0.064

Table 3.3: Parameters of silicon used in optical phonon scattering rate calculation.

Fig. 3.4 is the total (absorption + emission) optical scattering rate under various temperatures. As the temperature decreases, the scattering rate tends to be smaller. However, there is no obvious lowering as the temperature is below 50K.

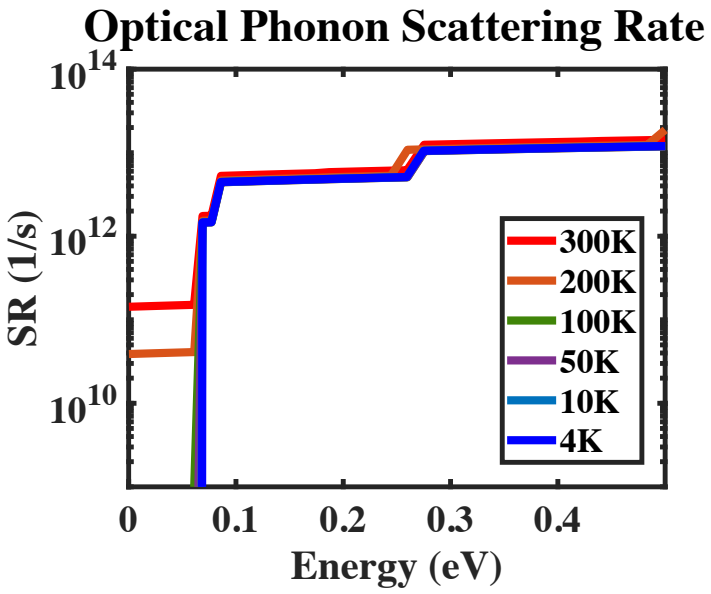

Figure 3.4: Optical phonon total scattering rate under different temperatures.

doi:10.6342/NTU202404100

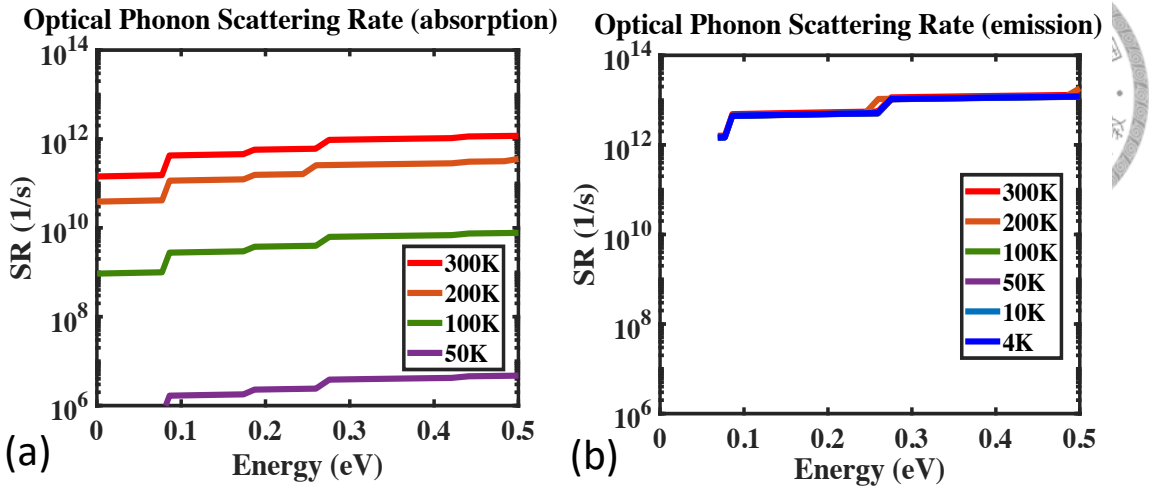

Figure 3.5: Optical phonon absorption (a) and emission (b) scattering rate under different temperatures. (a) the scattering rates under 50K are smaller than 1.0×10^6 s^{-1}. Thus, they are not plotted in (a).

This is because of the saturation of the phonon occupation in the emission mode, and the absence of the absorption mode at low temperature. In Fig. 3.5, we can see that the absorption scattering rate drops as the temperature lowers, and at 50 K, the absorption scattering rate is below 1.0×10^5 s^{-1}. On the other hand, the emission scattering rate does not decrease too much with the temperature changes. From Eq. 2.7 and Eq. 2.3, we realize that the emission scattering rate gradually closes to the condition that phonon occupation term equals one as temperature lowering. However, absorption is influenced by the phonon occupation declining with the temperature changes. To sum up, within the temperature decrease, the optical phonon scattering rate is dominated by the emission mechanism, and it will converge to the result that the phonon occupation term equals one in the emission scattering rate calculation.

3.2.3 Equivalent Intervalley Scattering

After interacting with the phonon, the electron has the probability to scatter into other valleys and follows the energy and momentum conservation. In bulk silicon, there are four

doi:10.6342/NTU202404100

degeneracy for f-type scattering and one degeneracy for g-type scattering. However, in the silicon (110) confinement system, there are two degeneracies for f-type scattering due to the confinement effect. Also, by applying the deformation potential theory, the equivalent intervalley scattering rate can be estimated with the parameters in Table. 3.4.

Scattering type	$D_{eq} \times 10^8 (eV/m)$	$\hbar\omega_{eq}(eV)$
g-type	0.5 / 0.8 / 11.0	0.012 / 0.019 / 0.062
f-type	0.3 / 2.0 / 2.0	0.019 / 0.047 / 0.059

Table 3.4: Parameters of silicon used in equivalent intervalley scattering rate calculation. [9]

There are three phonon types separately attributed to g-type and f-type scattering. They are oriented from the different LA, TA, LO, and TO phonon modes with different phonon wavevectors (Fig. 3.6).

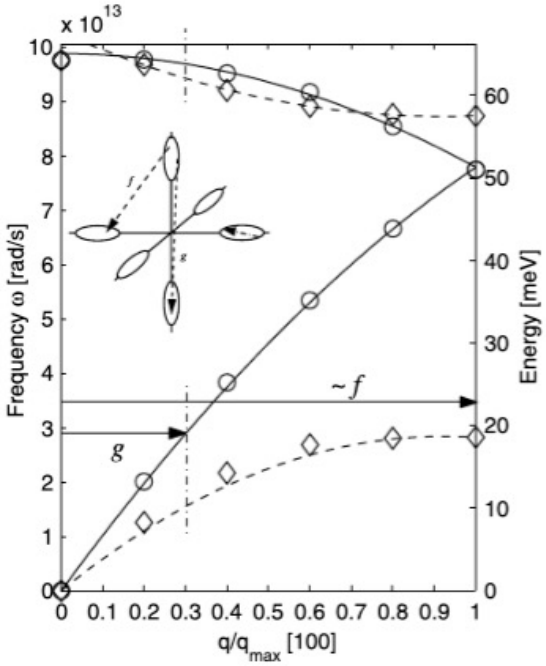

Figure 3.6: Equivalent intervalley scattering with different phonon wavevector [20]. The change of phonon wavevector of g-type transition required 0.3 times zone edge magnitude, and f-type transition required one time.

Fig. 3.7 is the total scattering rate of the g-type and f-type scattering. As the temperature declines, the total scattering rate becomes smaller. The abrupt scattering rate in-

doi:10.6342/NTU202404100

crement in the low electron energy is due to the activation of the different phonon modes. Fig. 3.8 shows the g-type and f-type scattering rates separately. g-type has the higher scattering rate due to the larger deformation potential parameter D_{eq} and the degeneracy reduction (four becomes two) of f-type scattering. Additionally, the same phenomenon of emission scattering gradually dominates the scattering rate, and the magnitude close to the phonon occupation term equals one as the temperature decreases (Fig. 3.9).

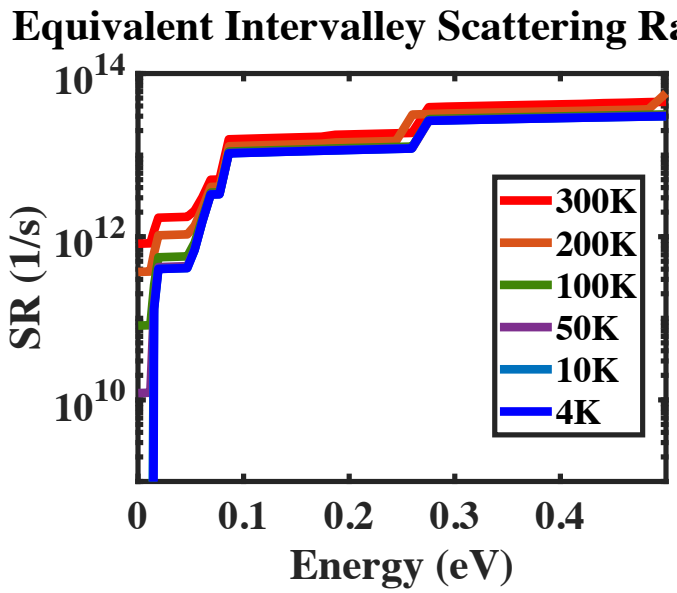

Figure 3.7: Equivalent intervalley total scattering rate.

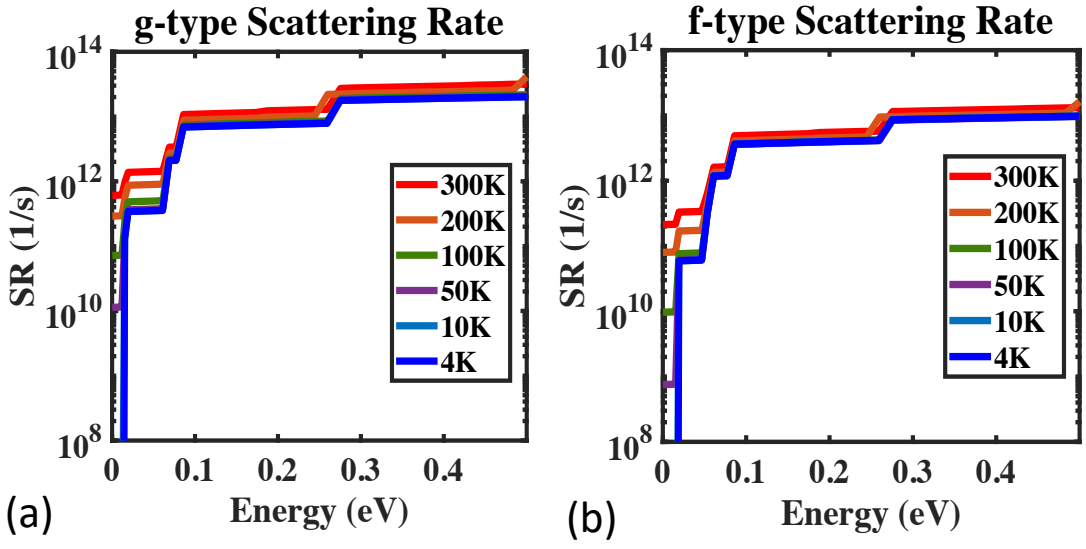

Figure 3.8: Equivalent intervalley g-type and f-type scattering rate.

doi:10.6342/NTU202404100

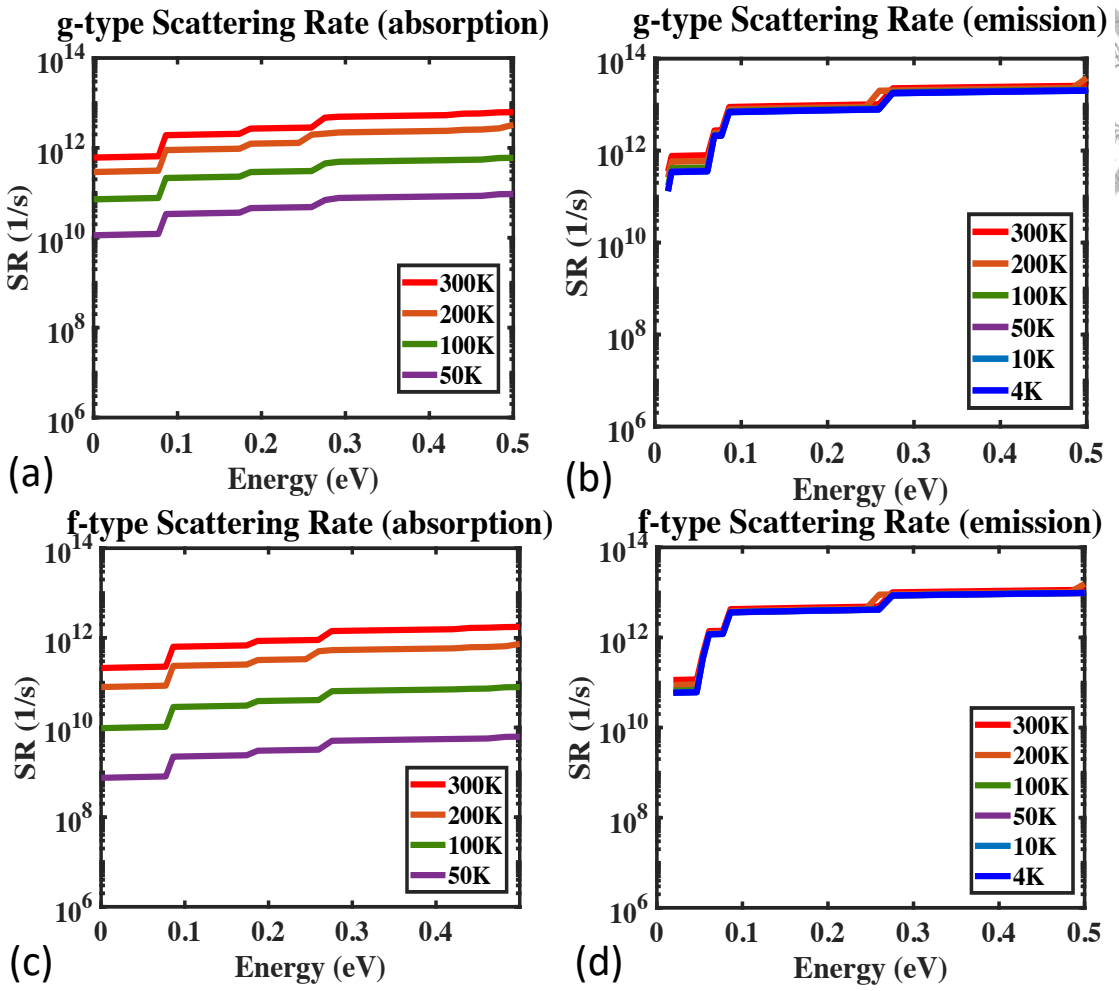

Figure 3.9: Equivalent intervalley (a) g-type absorption, (b) g-type emission, (c) f-type absorption, and (d) f-type emission scattering rate.

3.2.4 Remote Phonon Scattering

To have a better gate control ability in the device, the high-κ materials are applied as the dielectric layer in the device. The remote phonon scattering is induced by this high dielectric constant material. In this study, we discuss the remote phonon scattering effect by comparing the conditions that two different oxide materials (SiO_2 and HfO_2) as the dielectric. Table. 3.5 shows the parameters used in remote phonon scattering rate calculation. Remote phonon is induced from the transversal optical phonon of these materials.

doi:10.6342/NTU202404100

Material	ϵ_r^0 (ϵ_0)	ϵ_r^i (ϵ_0)	ϵ_r^∞ (ϵ_0)	$\hbar\omega_{TO}^1(eV)$	$\hbar\omega_{TO}^2(eV)$
SiO_2	3.90	3.36	2.40	0.055	0.138
HfO_2	22.00	6.58	5.03	0.012	0.048

Table 3.5: Remote phonon parameters of the materials used as the dielectric. ϵ_r^0, ϵ_r^i, and ϵ_r^∞ are low-frequency, intermediate-frequency and high-frequency permittivity, respectively. [11, 21]

From the FinFET structure, we can simplify our simulation into the double gates condition. That is, the silicon channel is sandwiched by the top and bottom dielectrics. The material of both sides oxide is the same. The width of the channel is 5 nm, and the thickness of the oxide is 1 nm. Fig. 3.10 is the remote phonon scattering rate of both sides oxides are HfO_2 and SiO_2. Compared with oxides in are SiO_2 case, the HfO_2 one has a much higher scattering rate. This is because of the large dielectric constant at low frequency. The ratio between $(\epsilon_{top}^0 + \epsilon_{bot}^\infty)$ and $(\epsilon_{top}^{int} + \epsilon_{bot}^\infty)$ becomes larger, and leads to the calculation in remote phonon mode (Eq. 2.13 and Eq.2.14) larger than the SiO_2 case.

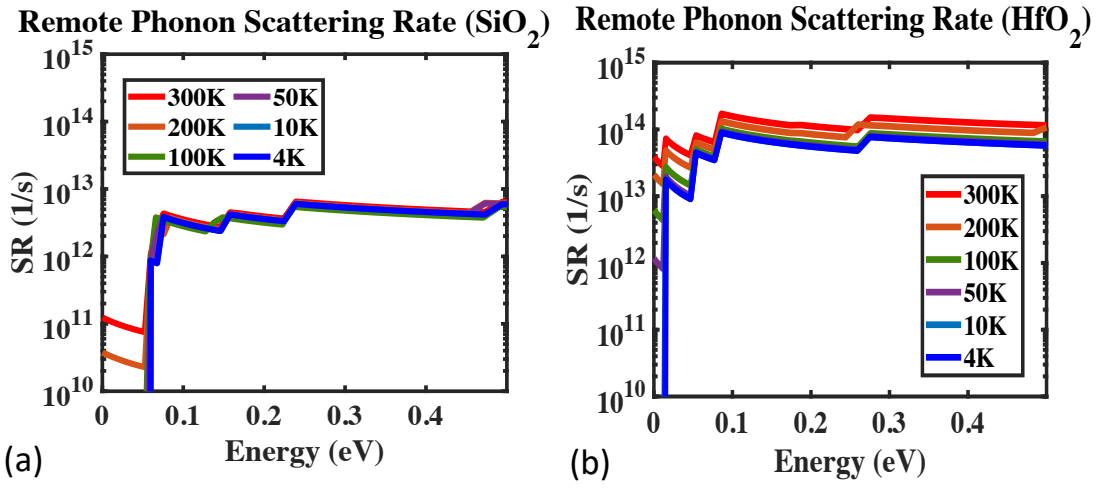

Figure 3.10: Remote phonon scattering rate of (a) SiO_2 and (b) HfO_2.

doi:10.6342/NTU202404100

3.2.5 Field-dependent Mobility in Electron-phonon Scattering

Due to the absence of the emission mechanisms in acoustic phonon scattering, in our Monte Carlo simulation, the electron is accelerated and scattered to the high energy states. That is, the scattering rate corresponding to the electron is too high, and this condition is not profitable to be simulated singly in the Monte Carlo method. Therefore, we add acoustic phonon scattering with other scattering mechanisms that have the emission process to estimate the electron mobility. In this section, the mobility considered in the aforementioned phonon scattering mechanism is discussed.

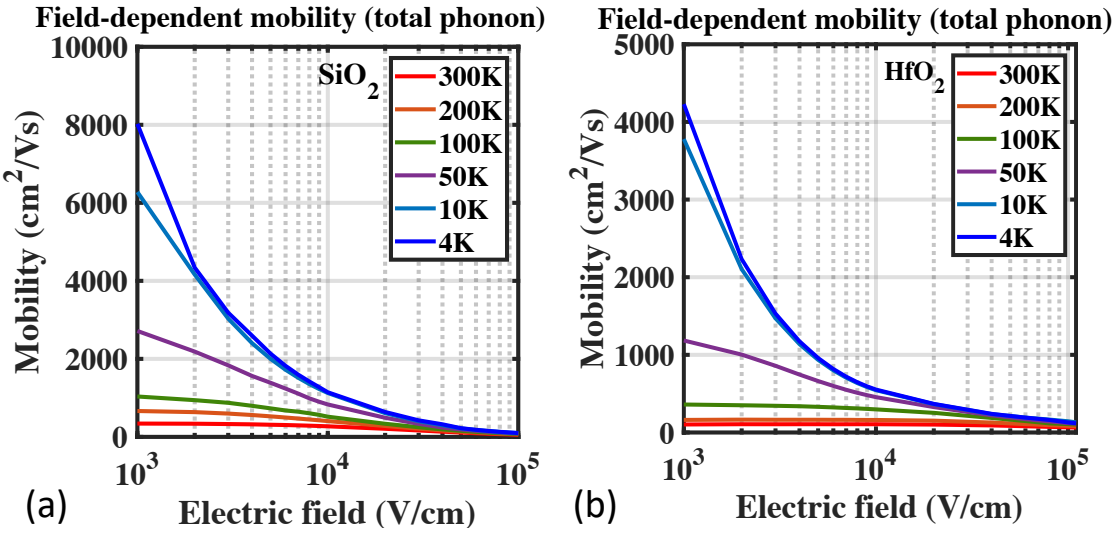

Figure 3.11: The field-dependent mobility of total phonon scattering mechanisms with temperatures. Total phonon means acoustic phonon scattering, optical phonon scattering, equivalent intervalley scattering, and remote phonon scattering are considered. (a) SiO_2 is considered as the dielectric layer in remote phonon calculation. (b) HfO_2 is considered as the dielectric layer in remote phonon calculation.

Fig. 3.11 is the field-dependent mobility of total phonon scattering mechanisms. In the room temperature case, if the electric field is not large enough unstable field-dependent mobility occurs due to the diffusion motion. Therefore, it is crucial to determine which electric field is profitable to extract the mobility. In our case, the electric field of 1000 V/cm is chosen, and the mobility in this condition is recorded. Fig. 3.12 is the field-

doi:10.6342/NTU202404100

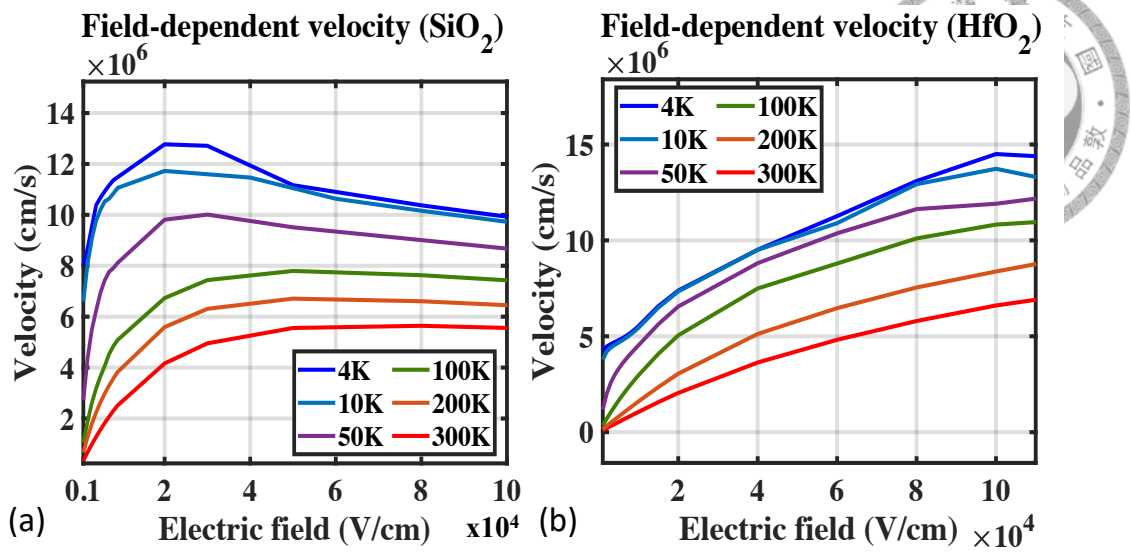

Figure 3.12: The field-dependent velocity of the phonon-related mechanisms with temperatures. In the remote phonon calculation, (a) SiO_2 is the dielectric material and (b) HfO_2 is the dielectric material.

dependent velocity of the phonon-related mechanisms mechanisms at different temperatures. As the temperature decreases, the velocity increases. This trend is due to the reduced phonon scattering at lower temperatures. Additionally, as the electric field increases, the velocity reaches saturation due to higher scattering corresponding to higher electron energy.

Fig. 3.13 is the summary of the mobility changing with the temperature of the phonon-related scattering transitions. In the remote phonon calculation, the dielectric layer is considered as HfO_2. The mobility is extracted under the electric field 1000 V/cm. Firstly, the intrinsic phonon scattering is discussed. Intrinsic phonon means the phonon is oriented from the material itself. There are acoustic phonon scattering, optical phonon scattering, and equivalent intervalley scattering. From the result, we observe that acoustic phonon scattering dominates since the purple line has an obvious drop, compared with the orange and blue lines. That is, acoustic phonon scattering is more severe than optical phonon scattering and equivalent intervalley scattering.

doi:10.6342/NTU202404100

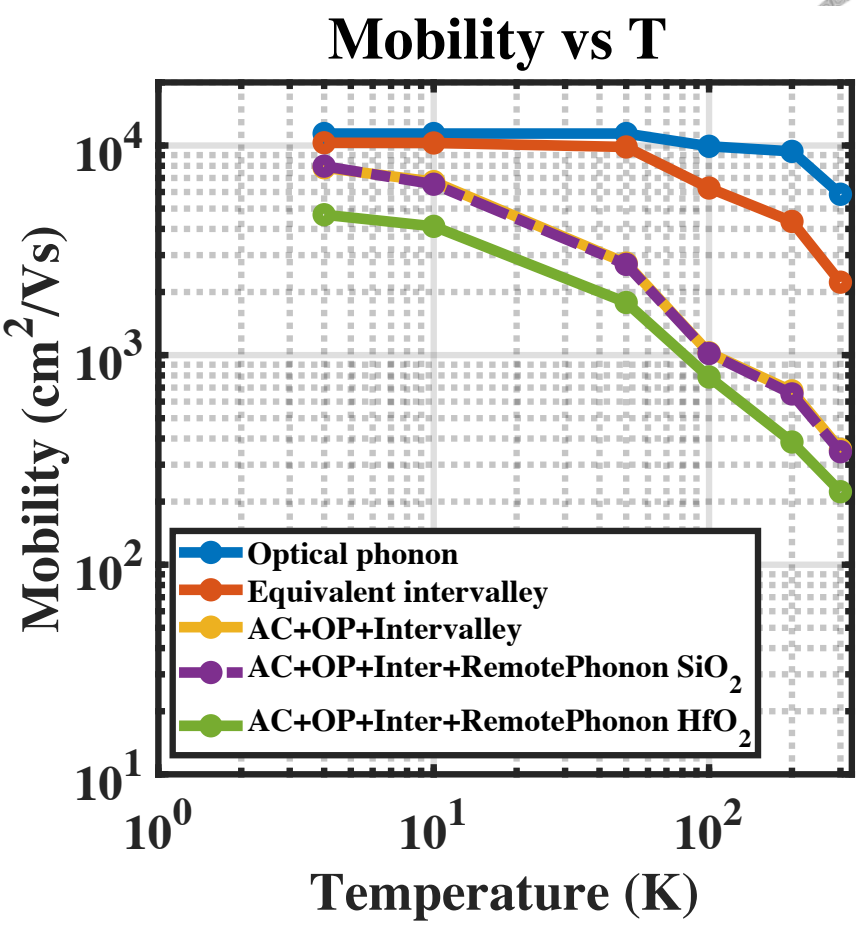

Figure 3.13: The mobility of various phonon scattering mechanisms with temperatures. In the remote phonon calculation, HfO_2 is the dielectric material.

However, in terms of extrinsic phonon, which means remote phonon is also taken into account, the remote phonon takes the role. The purple and blue lines in Fig. 3.13 are the simulation that considers remote phonon. The sharp decrement of mobility represents the remote phonon from HfO_2 induces the scattering. Therefore, the choice of dielectric material is important in carrier transport property.

3.3 Surface Roughness Scattering

Surface roughness scattering occurs when electrons move around the interface of two materials. The imperfection surface causes fluctuations in the potential energy landscape,

doi:10.6342/NTU202404100

leading to scattering events that affect the motion of the electrons, and this mechanism is independent of the temperature. Eq. 2.23 represents the roughness degree of the interface, and it is simplified by using the Gaussian equation. Fig 3.14 shows the roughness in 2D space with different Gaussian broadening magnitudes (λ in Eq. 2.23).

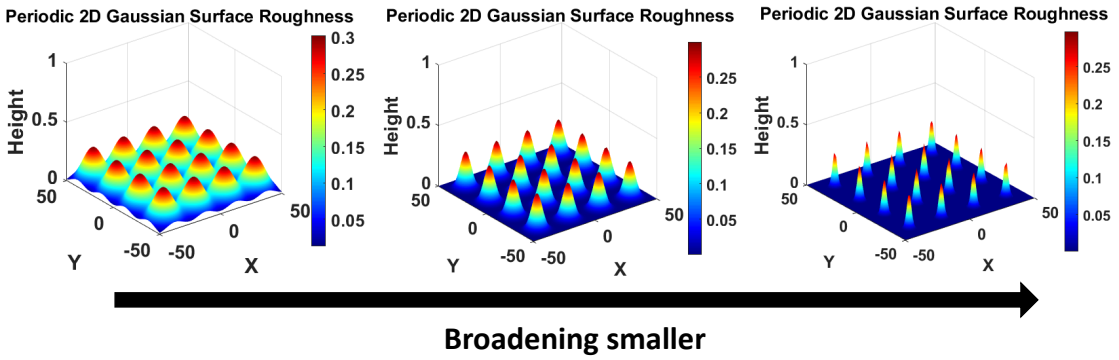

Figure 3.14: The schematic of the surface roughness in 2D space simplified by Gaussian equation. The different broadening describes the various roughness magnitudes.

In this part, the degree of the roughness is changed, and the electron distribution is assumed the same. That is, our discussion can focus on the relation between roughness parameters and scattering rate. The maximum potential change is the difference between the conduction band edge of silicon and HfO_2, and it is set as 1.3 eV (δU) in our calculation. Fig. 3.15 is the scattering rate result of different roughness parameters. As the λ is smaller, it means the broadening of the roughness is larger. Therefore, when the carrier transports in this 2D space, it has more possibility to meet the roughness island and this leads to the scattering rate increases.

3.3.1 Field-dependent Mobility in Surface Roughness Scattering

After calculating the surface roughness scattering rate, we discuss the effect of this mechanism on electron mobility. Fig. 3.16 is the result. The phonon mobilities are also shown in this figure. The below blue and green curves are the mobility with different

doi:10.6342/NTU202404100

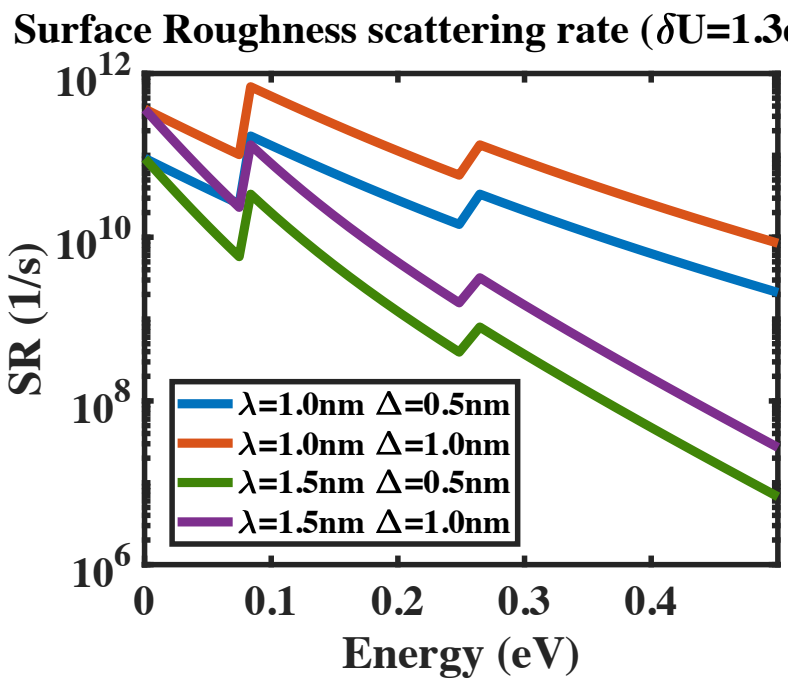

Figure 3.15: The surface roughness scattering rate with different λ and Δ.

degrees of surface roughness. We compare the mobility changes with and without considering surface roughness. In the remote phonon part, HfO_2 is chosen as the dielectric layer. From this plot, we can realize that after surface roughness is added to the system, the mobility decreases at low temperatures. However, at room temperature, the mobilities are close to the purple curve, which represents the total phonon mobility. This phenomenon indicates that phonon-related scattering still dominates at room temperature, but as the temperature declines, the effect of surface roughness takes place.

3.4 Remote Coulombic Scattering

Remote Coulombic scattering is induced from the charges located in the oxide or at the oxide-semiconductor interface. Due to the propagation of the Coulomb potential, the transport property of the carrier in the channel is influenced. Since the Coulomb force is related to the distance between the oxide charges and channel carriers, knowing the distri-

doi:10.6342/NTU202404100

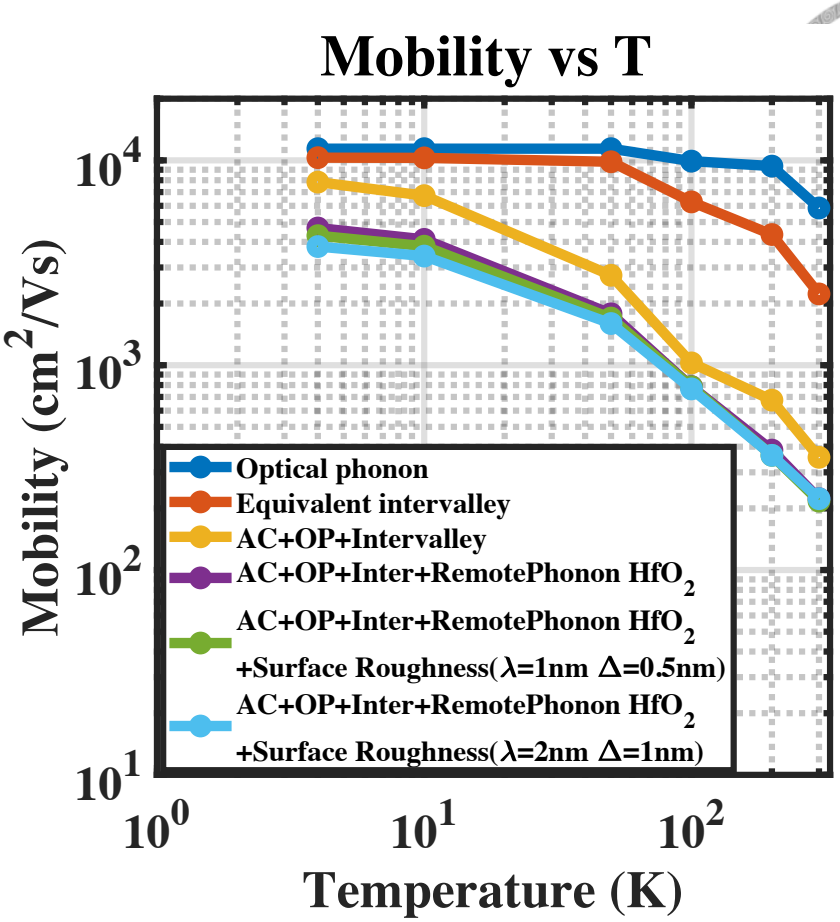

Figure 3.16: The mobility of phonon-related scattering mechanisms and the surface roughness with different roughness parameters.

bution of the carriers in the channel is vital. Therefore, in the remote Coulombic scattering rate calculation, the wavefunction is used to calculate the integral of Coulomb potential and the carrier distribution. In terms of the following calculation, we choose a similar 2D electron gas density in the inversion layer (N_{inv}) under temperatures (around 1.0×10^{12} cm^{-2}). As the N_{inv} is set, the magnitude of the screening effect is fixed. Therefore, we can focus on the relation between oxide fixed charge density and the scattering rate. A detailed discussion of the carrier density and screening effect is in session 3.7.

Fig. 3.17 shows the scattering rate with different oxide fix charge densities (N_{fix}). The position of the fixed charge in both cases is set as 1 nm away from the interface. From the result, we can observe the scattering rate rise as the N_{fix} increases due to more

doi:10.6342/NTU202404100

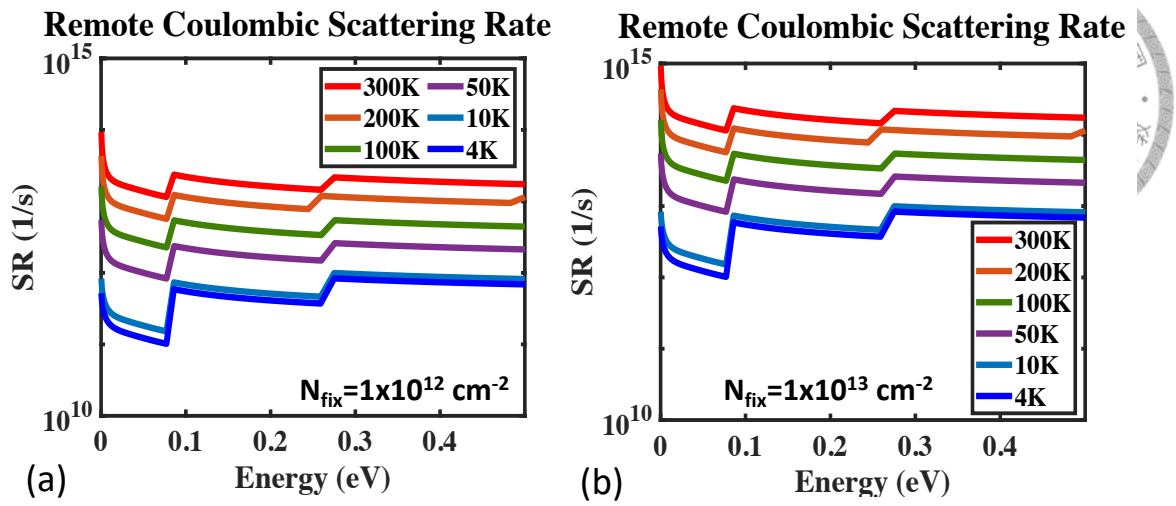

Figure 3.17: The Scattering rate of remote Coulombic scattering with $N_{fix} = 1.0 \times 10^{12}$ cm^{-2} and $N_{fix} = 1.0 \times 10^{13}$ cm^{-2} at various temperatures.

charges form the Coulomb potential. Besides, the decrement of the scattering rate as the temperatures lowered can be observed. This phenomenon results from the increment of the screening effect at low temperatures. In Eq. 2.18, the second term on the right-hand side, which represents the screening effect increases, and this leads to the scattering potential being smaller. Therefore, the scattering rate decreases.

3.4.1 Field-dependent Mobility in Remote Coulombic Scattering

After calculating the scattering rate, we further investigate the influence of remote Coulombic scattering. We compare the mobility decrement before and after considering the remote Coulombic scattering. Fig. 3.18 is the mobility result considering the remote Coulombic scattering.

Here, the HfO_2 is used as the dielectric layer to calculate the remote phonon scattering. The surface roughness parameters used in the simulation are $\lambda = 1.0$ nm and $\Delta = 0.5$ nm. After considering the remote Coulombic scattering, the mobility declines in low temperatures. As the $N_{fix} = 1.0 \times 10^{13}$ cm^{-2}, the drop occurs. As the temperature

doi:10.6342/NTU202404100

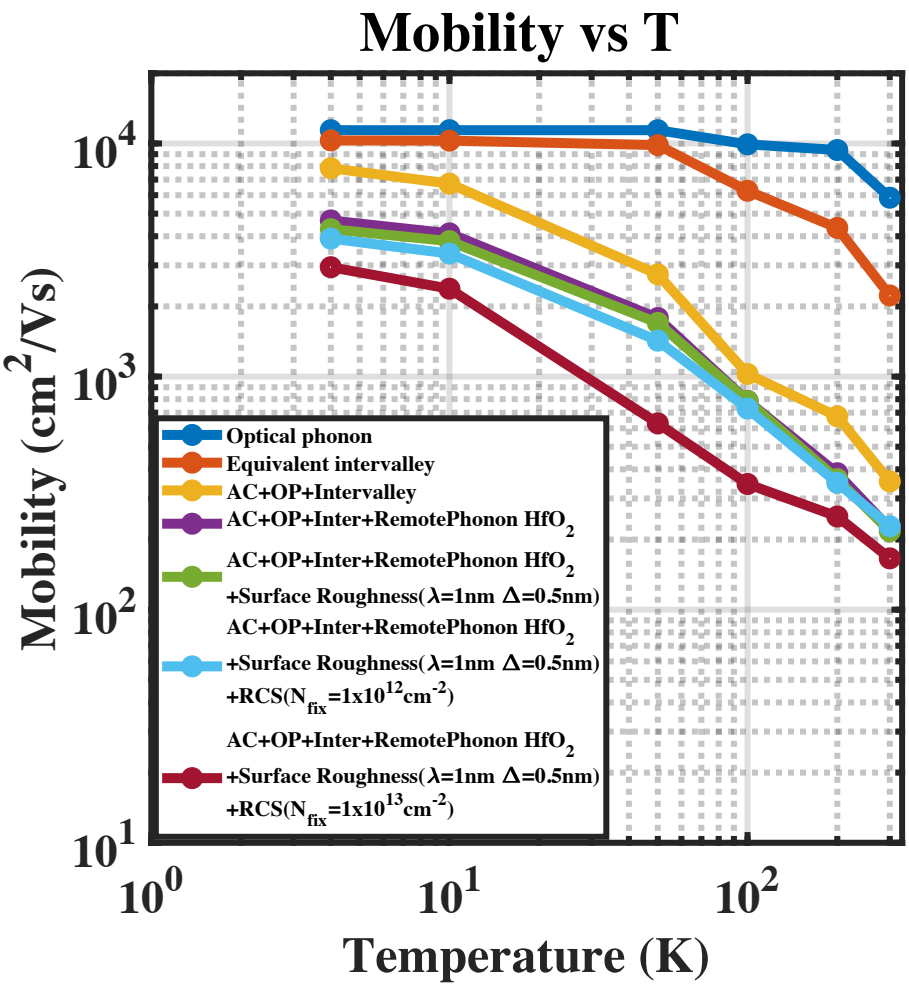

Figure 3.18: Mobility of the phonon-related scattering mechanisms and considering with the remote Coulombic scattering which $N_{fix} = 1.0 \times 10^{12}$ cm^{-2} and 1.0×10^{13} cm^{-2} under temperatures.

close to 300K, the mobility merges with the result that only considers phonon. That is, phonon-related scattering is the primary factor at room temperature.

3.5 Impurity Scattering

The physics of impurity scattering is similar to the remote Coulombic scattering. The scattering potential is formed by ionized impurities due to the Coulomb force. Compared with the remote Coulombic scattering, the charges causing the potential located in the channel. Therefore, with the same fixed-charge concentration, the impurity scattering

doi:10.6342/NTU202404100

rate is larger than the remote Coulombic scattering rate. In the scattering rate estimation, the wavefunction is also needed, and it is used to calculate the integer with the scattering potential formed by the ionized impurity.

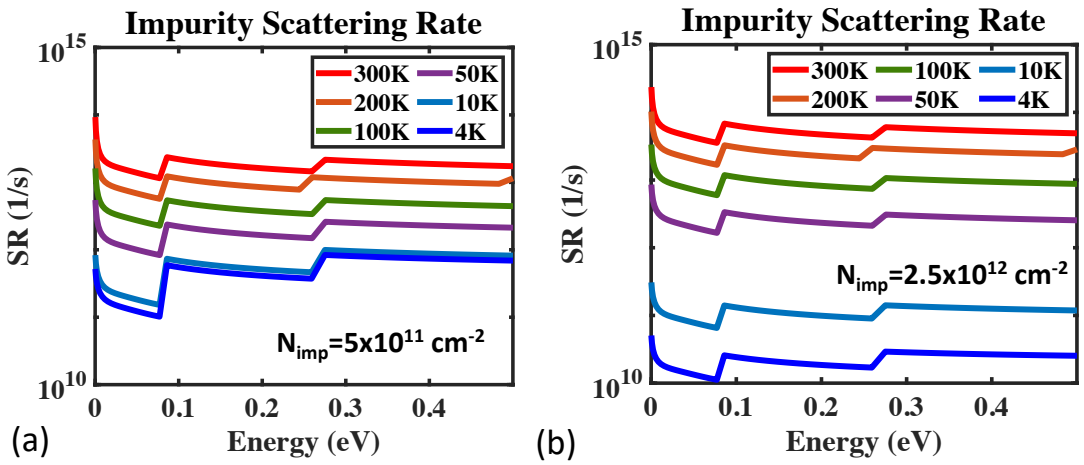

Figure 3.19: The Scattering rate of impurity scattering with $N_{imp} = 5.0 \times 10^{11}$ cm^{-2} and $N_{imp} = 2.5 \times 10^{12}$ cm^{-2} at various temperatures.

Fig. 3.19 is the impurity scattering rate with the impurity concentration is 1.0×10^{18} cm^{-3} and 5.0×10^{18} cm^{-3}. These values should be normalized by the device width of 9.0 nm. Therefore, the impurity concentration are 5.0×10^{11} cm^{-2} and 2.5×10^{12} cm^{-2}.The similar 2D electron gas density in the inversion layer (N_{inv}) under temperatures (around 1.0×10^{12} cm^{-2}) are chosen. First, the scattering rate increment with the higher impurity concentration can be observed. Further, the scattering rate is smaller as the temperature decreases, due to the screening effect being stronger (Eq. 2.18) at low temperatures.

3.5.1 Field-dependent Mobility of Impurity Scattering

After calculating the scattering rate, we further investigate the effect of impurity scattering. We compare the mobility changes with and without the impurity scattering. Fig. 3.20 is the mobility result with the impurity scattering. In remote phonon calculation, HfO_2 is used as the dielectric layer. The surface roughness parameters used in the simu-

doi:10.6342/NTU202404100

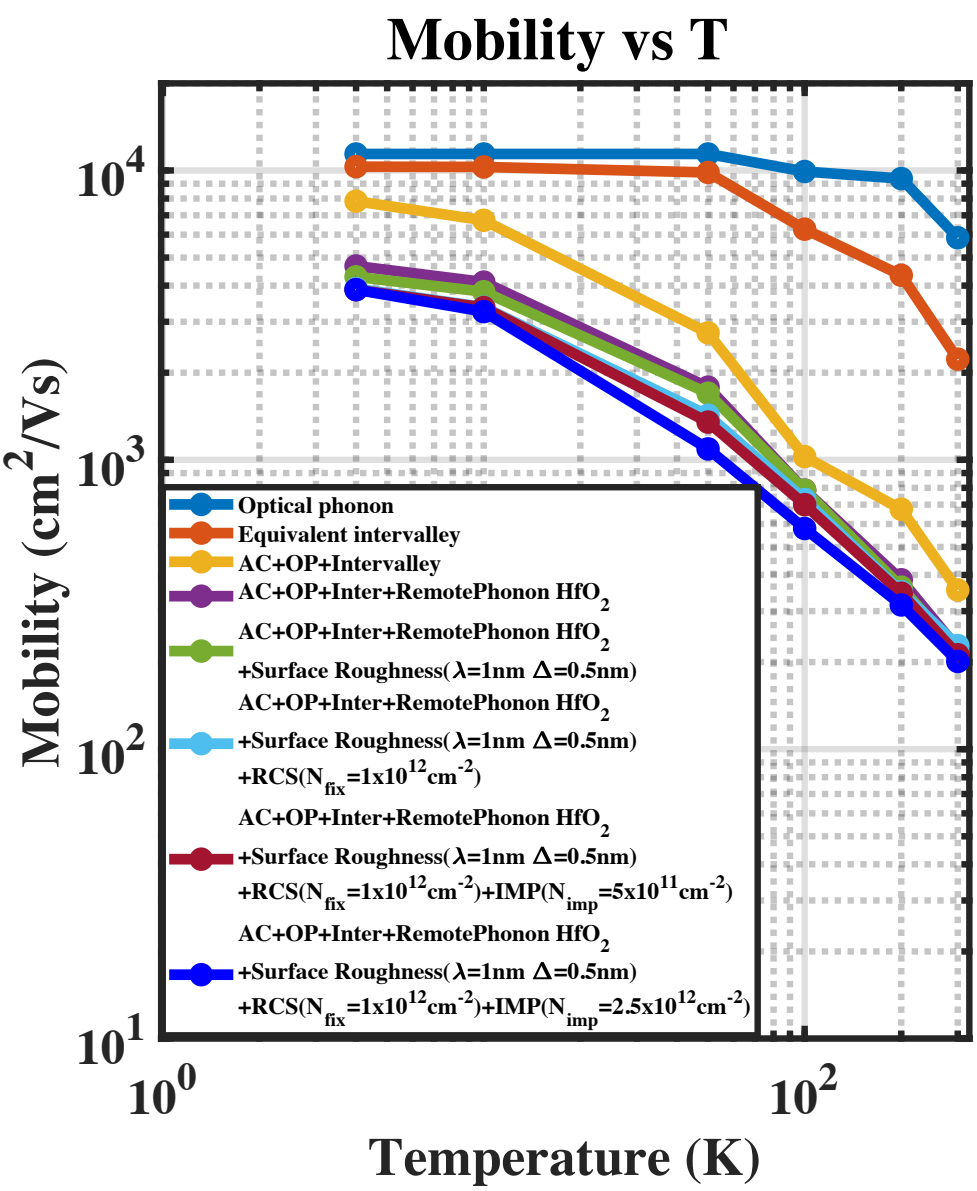

Figure 3.20: Mobility of the phonon-related scattering mechanisms and considering with the impurity scattering which $N_{imp} = 5.0 \times 10^{11}$ cm^{-2} and 2.5×10^{12} cm^{-2} under temperatures.

lation are $\lambda = 1.0$ nm and $\Delta = 0.5$ nm. The fixed charge density in remote Coulombic scattering is set as 1.0×10^{12} cm^{-2}, since 1.0×10^{13} cm^{-2} is too large to observe the effect of impurity scattering. From the results, we can observe that the lower three curves (light-blue, blue, and brown) merge as the temperature approaches room temperature. At low temperatures, impurity scattering slightly influences mobility under these circumstances, since the impurity density is similar or lower than the fix charge density in remote Coulom-

doi:10.6342/NTU202404100

bic scattering.

3.6 Total Mobility with Device 2D-DDCC Simulation

In this section, we connect the 2D device simulation result and the aforementioned scattering mechanisms calculation. To begin with, we use the 2D-DDCC to calculate the 2D band diagram of the device under the different gate voltage and at various temperatures. Next, solve the Schrodinger equation to obtain the wavefunctions based on the band diagram of the device. Further, applying the wavefunctions results in the scattering rate calculation. Finally, perform the Monte Carlo method to estimate the total mobility of electrons in the device under different gate voltages and at various temperatures.

3.6.1 2D Simulation Structure

Based on Fig. 3.1, we build a 2D device simulation to calculate the band diagram of the region around the gate. This region is simplified as a double-gate transistor (Fig. 3.21). The doping concentration used in the simulation is shown in the figure. The oxide region is used SiO_2 and HfO_2 in the further discussion.

3.6.2 Wavefunction Results

According to the above simulation structure, the gate bias is applied. Then, the inversion layer is formed, and electrons can transport through the channel. Further, the wavefunctions in the different inversion layers under temperatures are solved. Based on these wavefunctions, the scattering rate can be calculated under each circumstance. The result with the same temperature is compared together to let us investigate the relation

doi:10.6342/NTU202404100

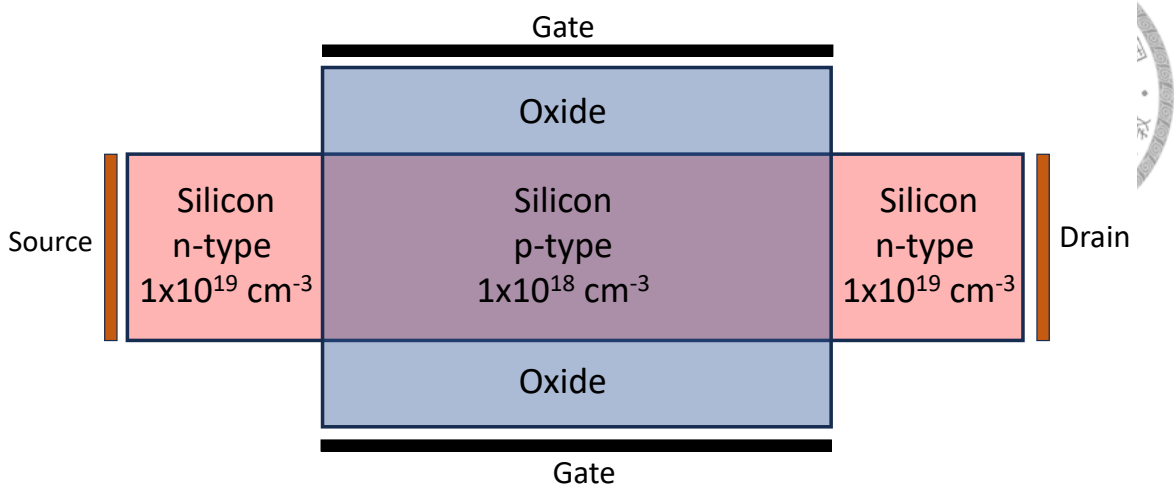

Figure 3.21: 2D simulation structure.

between mobility and the inversion concentration.

Fig. 3.22 is the wavefunction result under the different temperatures and inversion concentration is 1.0×10^{12} cm^{-2} and 5.0×10^{12} cm^{-2}.

3.6.3 Scattering Rate under Temperatures with Various Inversion Layer Concentration

Based on the wavefunctions results in the last subsection, the scattering rates can be obtained as the calculation in sections 3.2 to 3.5. Fig. 3.23 is the surface roughness scattering rate with different inversion concentrations. From Eq. 2.24, the magnitude of the electron distribution around the surface is quite important to calculate the surface roughness scattering rate. Therefore, from this result, we can observe the scattering rate enhanced as the inversion concentration larger. That is, higher N_{inv} means more electrons distribute around the surface, and their motions have much probability of being influenced by the surface roughness.

Next, we discuss the changing of remote Coulombic scattering with various inversion

doi:10.6342/NTU202404100

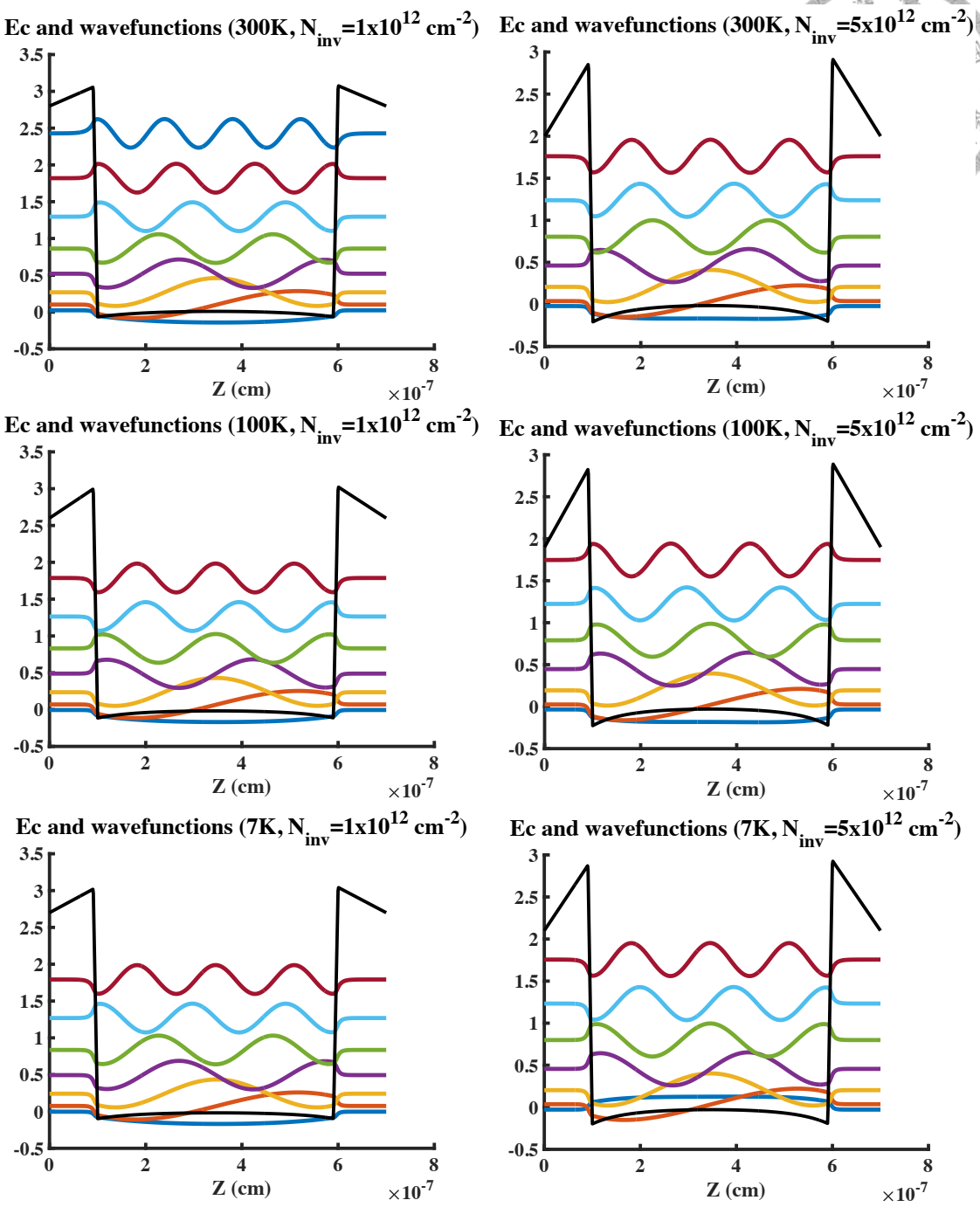

Figure 3.22: Wavefunctions result with inversion concentration is $1.0 \times 10^{12} cm^{-2}$ and $5.0 \times 10^{12} cm^{-2}$. The black solid line represents the conduction band.

densities. In Fig. 3.24, the fixed charge density is set as 1.0×10^{13} cm^{-2}, and the scattering rate decreases as the inversion layer concentration rises. This is because of the screening effect of the carriers in the channel. Higher N_{inv} represents the stronger screening effect; therefore, the less scattering events happen at higher N_{inv}.

doi:10.6342/NTU202404100

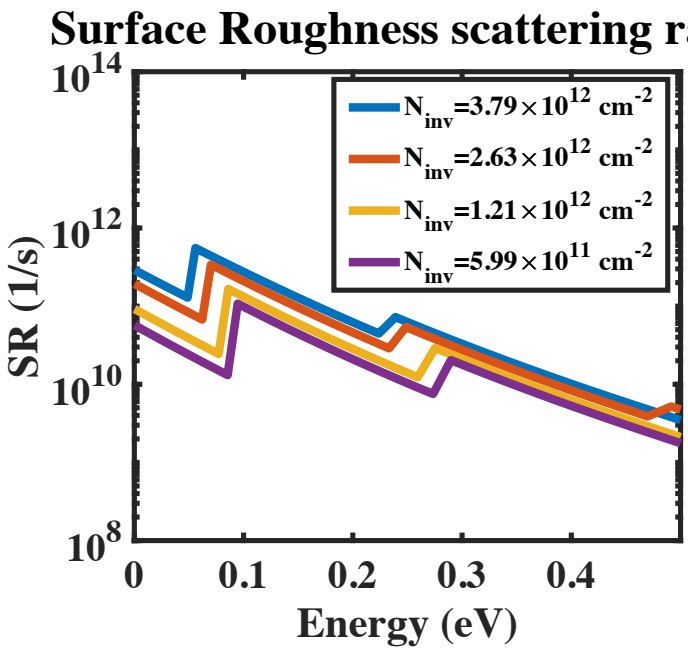

Figure 3.23: Surface roughness scattering rate ($\lambda = 1.0$ nm and $\Delta = 0.5$ nm) calculated from the wavefunctions with different inversion layer concentrations.

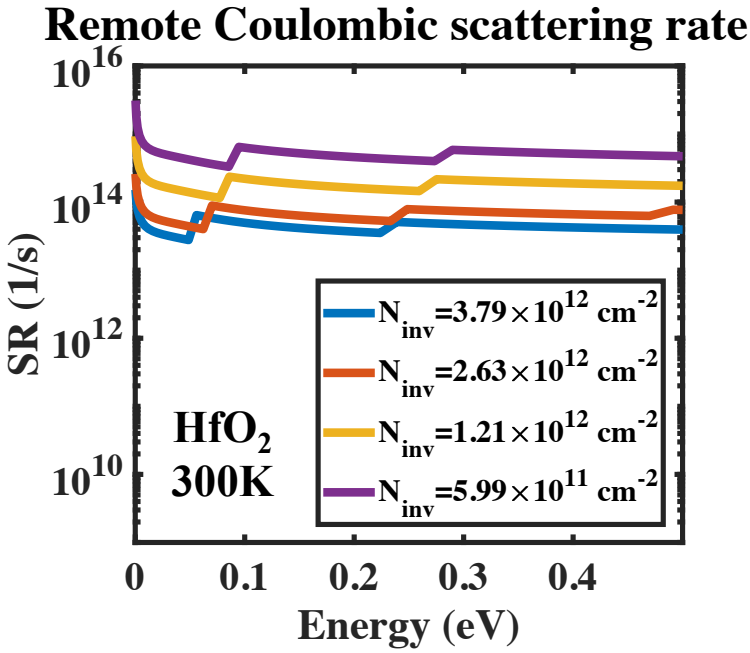

Figure 3.24: Remote Coulombic scattering rate ($N_{fix} = 1.0 \times 10^{13}\text{cm}^{-2}$) calculated from the wavefunctions with different inversion layer concentrations.

doi:10.6342/NTU202404100

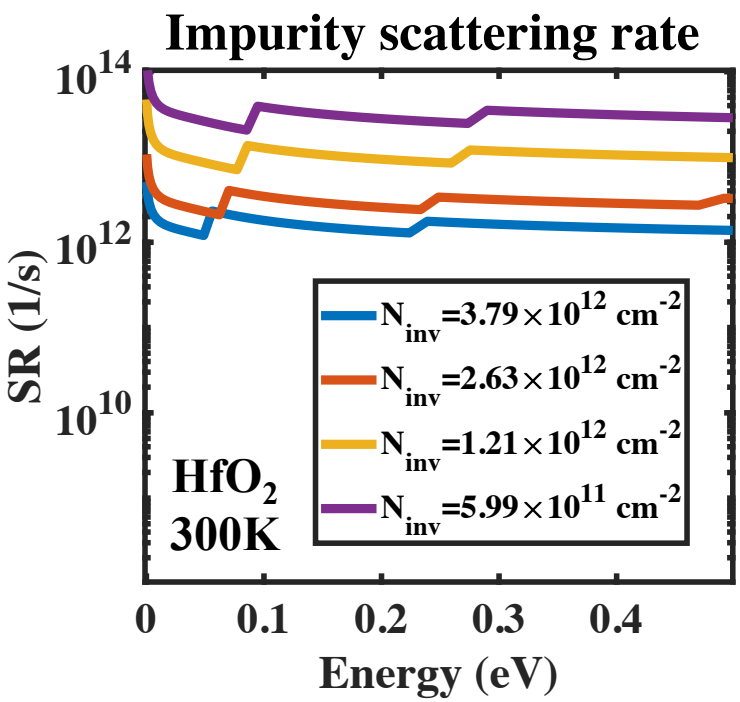

Figure 3.25: Impurity scattering rate ($N_{imp} = 5.0 \times 10^{11} \text{cm}^{-2}$) calculated from the wavefunctions with different inversion layer concentrations.

Moreover, the impurity scattering rate is also discussed. Fig. 3.25 is the impurity scattering with the different inversion layer density, and the impurity concentration is 5.0×10^{11} cm^{-2}. Similar to the tendency of remote Coulombic scattering rate, the impurity scattering is reduced as the N_{inv} increases. This phenomenon also resulted from the screening of the channel carriers.

3.6.4 Mobility under Temperatures with Different Inversion Layer Concentration

After calculating the scattering rate, the electron mobility can be obtained by the Monte Carlo method. The parameters set are the same as in the above discussion. Fixed charge density in the oxide is set as 1.0×10^{13} cm^{-2}, and impurity concentration is 5.0×10^{11} cm^{-2}. In terms of oxide, to reach the same EOT as SiO_2 is 1 nm, the thickness of HfO_2 is set as 6.15 nm. In surface roughness scattering, two sets of parameters are used.

doi:10.6342/NTU202404100

They are $\lambda = 1.0$ nm and $\Delta = 0.5$ nm for HfO_2 and $\lambda = 1.0$ nm and $\Delta = 0.2$ nm for SiO_2, by considering the energy difference between the surface of Si/HfO_2 (1.3 eV) and Si/SiO_2 (3.1 eV).

Fig. 3.26 is the summary of the mobility with different N_{inv} under temperatures. From the results, we can observe a downward concave trend of electron mobility with respect to N_{inv}. This phenomenon results from the competition between surface roughness scattering and remote Coulombic scattering. At lower inversion regions, the screening effect is weak, and the remote Coulombic scattering rate is higher. As the N_{inv} rises, the remote Coulombic scattering rate starts to decrease. On the other hand, the surface roughness scattering starts to increase, due to the higher electron distribution around the surface. During this process, the mobility reaches the highest value. Then, at the high N_{inv} region, the effect from surface roughness scattering takes place, and the influence from the remote Coulombic scattering is weakened.

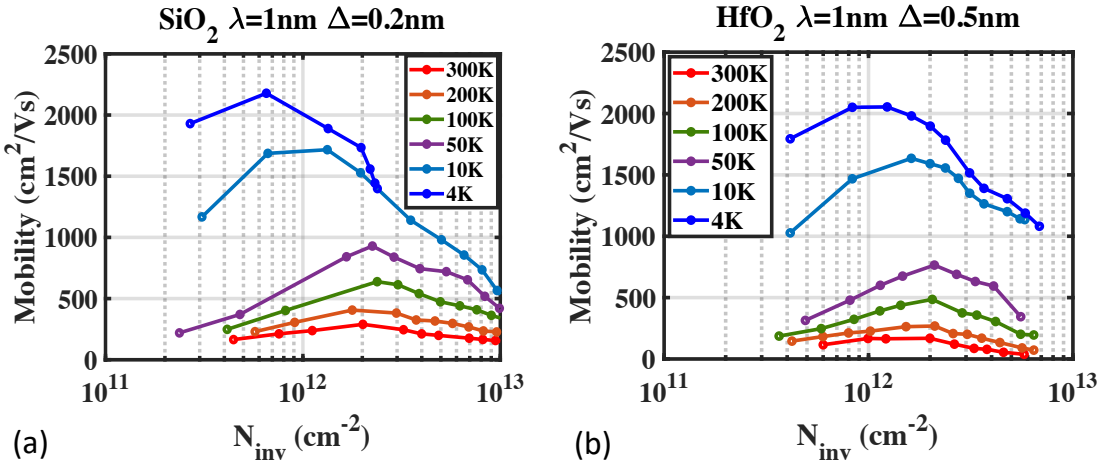

Figure 3.26: (a) Mobility of the system that dielectric layer is SiO_2. N_{fix} in remote Coulombic scattering is 1.0×10^{13} cm^{-2}. N_{imp} in impurity scattering is 5.0×10^{11} cm^{-2}. The parameters used in surface roughness calculation is $\lambda = 1.0$ nm and $\Delta = 0.2$ nm and (b) Mobility of the system that dielectric layer is SiO_2. N_{fix} in remote Coulombic scattering is 1.0×10^{13} cm^{-2}. N_{imp} in impurity scattering is 5.0×10^{11} cm^{-2}. The parameters used in surface roughness calculation is $\lambda = 1.0$ nm and $\Delta = 0.5$ nm.

Fig. 3.27 shows the overall scattering rate changes with N_{inv} under 50K and 300K

doi:10.6342/NTU202404100

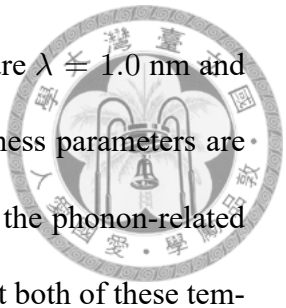

of SiO_2 is the dielectric layer and the surface roughness parameters are $\lambda = 1.0$ nm and $\Delta = 0.2$ nm and HfO_2 is the dielectric layer and the surface roughness parameters are $\lambda = 1.0$ nm and $\Delta = 0.5$ nm, respectively. To begin with, at 50K, the phonon-related scattering rate magnitudes are lower than those at 300 K. Moreover, at both of these temperatures, we can observe the competition between remote Coulombic scattering and surface roughness (red and blue curves) with different N_{inv}. At low N_{inv}, remote Coulombic scattering dominates. With the rising of N_{inv}, the surface roughness rate increases, and remote Coulombic scattering becomes lower. As the N_{inv} is larger, the surface roughness scattering rate reaches the magnitude of the remote Coulombic scattering rate. In terms of the ratio of these two mechanisms to the total scattering rate, since the phonon scattering rate is higher at 300K, the mobility change owing to the alternation of these two mechanisms is not that obvious, compared with the case under 50K. In addition, by comparing the different dielectric material cases, the higher remote phonon scattering can be observed in Fig. 3.27 (c) and (d). Notably, in the case of SiO_2, the effect of acoustic phonon scattering is more significant than that of remote phonon scattering.

Then, we discuss the scattering rates change with temperatures under different N_{inv}. Fig.3.28 shows the overall scattering rates change with temperatures with $N_{inv} \sim 1.0 \times 10^{12}$ cm^{-2} and 5.0×10^{12} cm^{-2}. To begin with, as the temperature decreases, except for surface roughness scattering, the scattering rates of all the other mechanisms decline. For phonon-related scattering, this is because of the less heat fluctuation. For remote Coulombic scattering and impurity scattering, this phenomenon is due to the higher screening effect in low temperatures. Moreover, by comparing Fig.3.28 (a) and (b), it can be seen that except for remote Coulombic scattering, impurity scattering, and surface roughness scattering, the relationship of other scattering mechanisms with temperature is not affected

doi:10.6342/NTU202404100

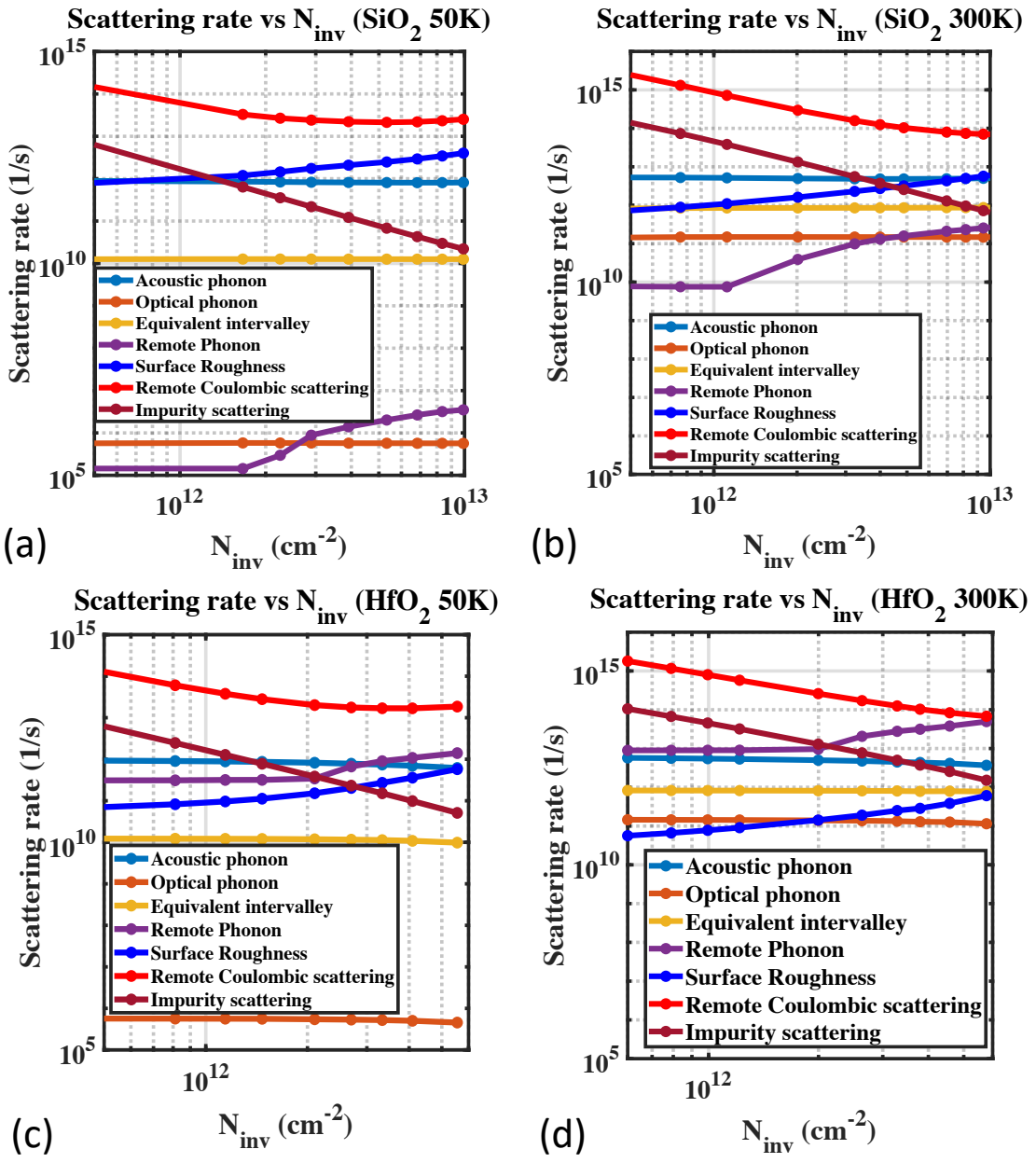

Figure 3.27: The overall scattering rates (electorn energy=0.001 eV) changing with N_{inv} at (a) 50K and (b) 300K. SiO_2 is used as the dielectric. The surface roughness parameters are set as $\lambda = 1.0$ nm and $\Delta = 0.2$ nm. (c) 50K and (d) 100K. HfO_2 is used as the dielectric. The surface roughness parameters are set as $\lambda = 1.0$ nm and $\Delta = 0.5$ nm.

doi:10.6342/NTU202404100

by changes in N_{inv} concentration. In addition, by comparing the different dielectric material cases, the larger remote phonon scattering rate can be observed in Fig.3.28 (c) and (d). The value is close to that of remote Coulombic scattering and surface roughness scattering, indicating that the effect of remote phonon scattering is significant under these circumstances.

To sum up, except for surface roughness scattering, all other scattering mechanisms vary with temperature. Additionally, the scattering mechanisms that are influenced by N_{inv} concentration include remote Coulombic scattering, impurity scattering, and surface roughness scattering. Under low-temperature conditions, the influence of surface roughness scattering, remote Coulombic scattering, and impurity scattering are evident, but the effect magnitude is related to the surface roughness, oxide charge density, and impurity concentration. At room temperature, phonon-related scattering dominates. Additionally, if considering the high-κ material, the effect of remote phonon is important. Take HfO_2 in our research for example, the remote phonon scattering rate is close to the remote Coulombic scattering rate and the surface roughness scattering rate.

doi:10.6342/NTU202404100

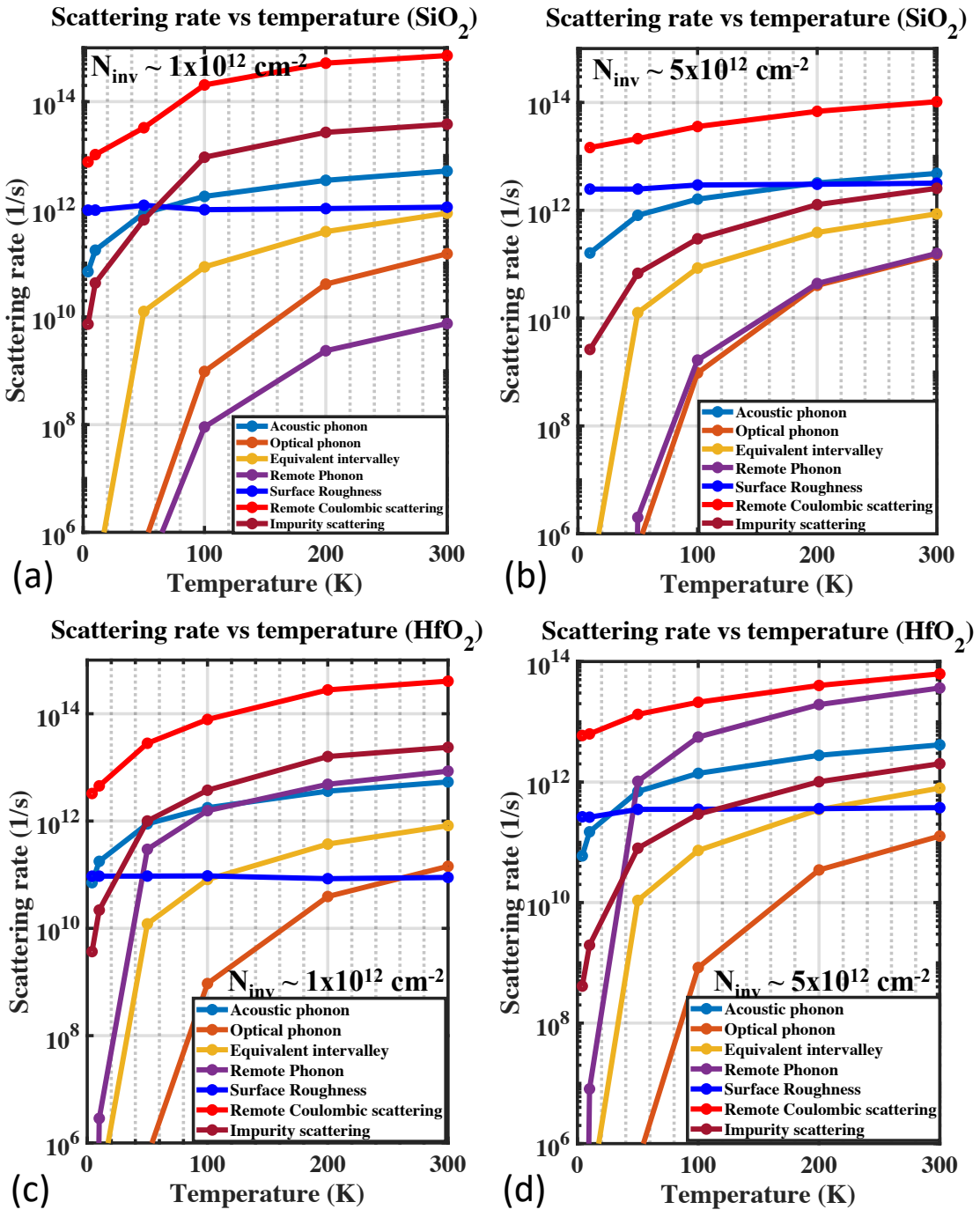

Figure 3.28: The overall scattering rates (electron energy=0.001 eV) changing with temperatures at (a) $N_{inv} \sim 1.0 \times 10^{12}$ cm^{-2} and (b) $N_{inv} \sim 5.0 \times 10^{12}$ cm^{-2}. SiO_2 is used as the dielectric. The surface roughness parameters are set as $\lambda = 1.0$ nm and $\Delta = 0.2$ nm. (c) $N_{inv} \sim 1.0 \times 10^{12}$ cm^{-2} and (d) $N_{inv} \sim 5.0 \times 10^{12}$ cm^{-2}. HfO_2 is used as the dielectric. The surface roughness parameters are set as $\lambda = 1.0$ nm and $\Delta = 0.5$ nm.

doi:10.6342/NTU202404100

Chapter 4

Conclusion

This thesis provides a study of the electron transport properties in silicon (110) confinement systems under the cryogenic. To begin with, we investigated various scattering mechanisms that impact electron mobility at low temperatures. Different from the room temperature, remote Coulombic scattering, impurity scattering, and surface roughness scattering should be taken into consideration in the low-temperature carrier transport property research. The scattering rate calculation model is built and the scattering rate of each scattering mechanism is acquired with different temperatures.

As the temperature decreases, the scattering effects from the phonon are reduced. For the mechanisms with the phonon energy emission, the scattering rate keeps at a certain magnitude, due to the saturation phonon occupation in the emission mode. On the other hand, the absorption scattering rate becomes quite small and can be neglected. Besides, the effect of the surface roughness scattering, remote Coulombic scattering and impurity scattering take place at low temperatures. At the same time, the screening effect from the channel carrier has to be considered. In the low channel carrier concentration condition, the remote Coulombic scattering rate and impurity scattering rate rise, and the electron

doi:10.6342/NTU202404100

mobility is reduced. However, if the screening effect is strong, the remote Coulombic scattering rate and impurity scattering rate become smaller and the surface roughness scattering plays a role.

In summary, this research has advanced our understanding of electron transport in silicon (110) confinement systems under the cryogenic. The cryogenic model from this study can be applied to calculate the carrier mobility of other systems like the device with other silicon orientations at low temperatures. Also, additional scattering mechanisms can be extended to this model to simulate the carrier transport properties of other promising materials in the cryogenic field.

doi:10.6342/NTU202404100

References

[1] Y. Quan, S. Yue, and B. Liao, "Impact of electron-phonon interaction on thermal transport: A review," *Nanoscale and Microscale Thermophysical Engineering*, vol. 25, no. 2, pp. 73–90, 2021.

[2] B. Liao, B. Qiu, J. Zhou, S. Huberman, K. Esfarjani, and G. Chen, "Significant reduction of lattice thermal conductivity by the electron-phonon interaction in silicon with high carrier concentrations: A first-principles study," *Physical review letters*, vol. 114, no. 11, p. 115901, 2015.

[3] N. Goldsman, L. Henrickson, and J. Frey, "A physics-based analytical/numerical solution to the boltzmann transport equation for use in device simulation," *Solid-state electronics*, vol. 34, no. 4, pp. 389–396, 1991.

[4] C. Jacoboni and L. Reggiani, "The monte carlo method for the solution of charge transport in semiconductors with applications to covalent materials," *Reviews of modern Physics*, vol. 55, no. 3, p. 645, 1983.

[5] N. Serra and D. Esseni, "Mobility enhancement in strained nn -finfets: Basic insight and stress engineering," *IEEE Transactions on Electron Devices*, vol. 57, no. 2, pp. 482–490, 2010.

doi:10.6342/NTU202404100

[6] D. Esseni, P. Palestri, and L. Selmi, *MOS transistors with arbitrary crystal orientation*, p. 348–365. Cambridge University Press, 2011.

[7] N. Hugenholtz, "Perturbation theory of large quantum systems," *Physica*, vol. 23, no. 1-5, pp. 481–532, 1957.

[8] S. L. Chuang, *Physics of photonic devices*. John Wiley & Sons, 2012.

[9] J. Singh, *Electronic and optoelectronic properties of semiconductor structures*. Cambridge University Press, 2007.

[10] Y. X. Ma, H. Su, W. M. Tang, and P. T. Lai, "Review on remote phonon scattering in transistors with metal-oxide-semiconductor structures adopting high-k gate dielectrics," *Journal of Vacuum Science & Technology B*, vol. 41, no. 6, 2023.

[11] M. V. Fischetti, D. A. Neumayer, and E. A. Cartier, "Effective electron mobility in si inversion layers in metal–oxide–semiconductor systems with a high-κ insulator: The role of remote phonon scattering," *Journal of Applied Physics*, vol. 90, no. 9, pp. 4587–4608, 2001.

[12] B. Hu, "Screening-induced surface polar optical phonon scattering in dual-gated graphene field effect transistors," *Physica B: Condensed Matter*, vol. 461, pp. 118–121, 2015.

[13] D. Esseni and A. Abramo, "Modeling of electron mobility degradation by remote coulomb scattering in ultrathin oxide mosfets," *IEEE Transactions on Electron Devices*, vol. 50, no. 7, pp. 1665–1674, 2003.

[14] F. Gámiz, J. López-Villanueva, J. Jiménez-Tejada, I. Melchor, and A. Palma, "A

doi:10.6342/NTU202404100

comprehensive model for coulomb scattering in inversion layers," *Journal of applied physics*, vol. 75, no. 2, pp. 924–934, 1994.

[15] S. Barraud, O. Bonno, and M. Cassé, "The influence of coulomb centers located in hfo2/sio2 gate stacks on the effective electron mobility," *Journal of Applied Physics*, vol. 104, no. 7, 2008.

[16] H. Jung, H. Ohtsuka, K. Taniguchi, and C. Hamaguchi, "Ionized impurity scattering rate for full band monte carlo simulation in heavily doped n-type silicon," *Journal of applied physics*, vol. 79, no. 5, pp. 2559–2565, 1996.

[17] E. B. Ramayya, D. Vasileska, S. Goodnick, and I. Knezevic, "Electron transport in silicon nanowires: The role of acoustic phonon confinement and surface roughness scattering," *Journal of Applied Physics*, vol. 104, no. 6, 2008.

[18] T. Ando, A. B. Fowler, and F. Stern, "Electronic properties of two-dimensional systems," *Reviews of Modern Physics*, vol. 54, no. 2, p. 437, 1982.

[19] S. M. Thomas, *Electrical characterisation of novel silicon MOSFETs and finFETs*. PhD thesis, University of Warwick, 2011.

[20] E. Pop, R. Dutton, and K. Goodson, "Detailed heat generation simulations via the monte carlo method," in *International Conference on Simulation of Semiconductor Processes and Devices, 2003. SISPAD 2003.*, pp. 121–124, IEEE, 2003.

[21] I.-T. Lin and J.-M. Liu, "Surface polar optical phonon scattering of carriers in graphene on various substrates," *Applied Physics Letters*, vol. 103, no. 8, 2013.

doi:10.6342/NTU202404100